

Design Implications of Chord Length and Number of Blades on Self-Starting Process in Vertical-Axis Wind Turbines

Faisal Muhammad¹, and Muhammad Saif Ullah Khalid^{1*}

¹Nature-Inspired Engineering Research Lab (NIERL), Department of Mechanical and Mechatronics Engineering, Lakehead University, Thunder Bay, ON P7B 5E1, Canada

*Corresponding Author, Email: mkhalid7@lakeheadu.ca

Abstract

Self-starting remains a key limitation of lift-driven vertical-axis wind turbines and is strongly influenced by geometric design choices that also govern steady-state performance. This work quantifies the roles of chord length and blade number on startup dynamics and the attained steady tip-speed ratio using two-dimensional URANS simulations of freely rotating Darrieus-type rotors. Two configuration families are examined, an equal-chord set in which three and five bladed turbines share the same chord length, and an equal-solidity set in which the chord length is reduced for the five blade turbines to match solidity with the three blade counterparts. Results are analyzed using the time evolution of tip-speed ratio, reduced-frequency measures to identify sustained unsteady intervals, vorticity-field diagnostics of dynamic stall vortex formation and detachment, and a torque decomposition into pressure and viscous moments. The results show that increasing number of blades can enhance early stage acceleration but generally lowers the steady tip-speed ratio by intensifying blade-vortex interaction in the downstream half cycle. Increasing chord length promotes self-starting by strengthening unsteady loading during the transition out of the low-speed regime, but also increases viscous losses and wake interaction, leading to lower the steady tip-speed ratio for self-starting high chord configurations. The role of viscous moments is also analyzed to quantify their contribution to self-starting behavior and to assess their influence on limiting the attainable operating state after self-starting. These findings provide design-relevant guidance on the startup–performance trade-off associated with c and N in freely accelerating VAWTs.

1 Introduction

Wind turbines can broadly be categorized into horizontal-axis wind turbines (HAWTs) and vertical-axis wind turbines (VAWTs) based on the rotational axis of their blades [1], each with distinct design characteristics and operational advantages. HAWTs, the more common type used in large-scale wind farms, offer high efficiency in open, unidirectional wind conditions due to their ability to align with the prevailing direction of wind. However, they require yaw mechanisms to track the wind, tall towers for mounting, and large clearances for blade rotation [2, 3]), increasing complexity and cost associated with installations. Moreover, HAWTs also pose a risk to avians and have vast geo-political and electromagnetic interference impact [4]. Contrarily, VAWTs rotate around a vertical axis and can function through the wind from all directions without reorientation, making them especially suitable for turbulent urban wind environments, lower wind speeds, and decentralized applications. Their ground-level generators simplify maintenance, and their compact design enables integration into rooftops, highways, and other constrained locations. Despite these advantages, VAWTs generally exhibit lower aerodynamic efficiency and have faced challenges with self-starting and dynamic stability.

Among VAWTs, two main types dominate, including Savonius and Darrieus turbines. The Savonius turbine is a drag-based design that offers excellent self-starting capabilities, simplicity, and robustness at lower angular velocities, but suffers from low efficiency due to significant drag forces. It is commonly used in low-power or remote applications, such as ventilation or water pumping [5]. On the other hand, the Darrieus turbine is a lift-based design that leverages aerodynamic forces to achieve

much higher efficiency at moderate to high tip-speeds ratios (λ). However, traditional Darrieus turbines are not inherently self-starting and may experience torque ripples and dynamic instabilities at certain operating ranges. Two representative models of VAWTs with three and five blades are shown in Fig. 1.

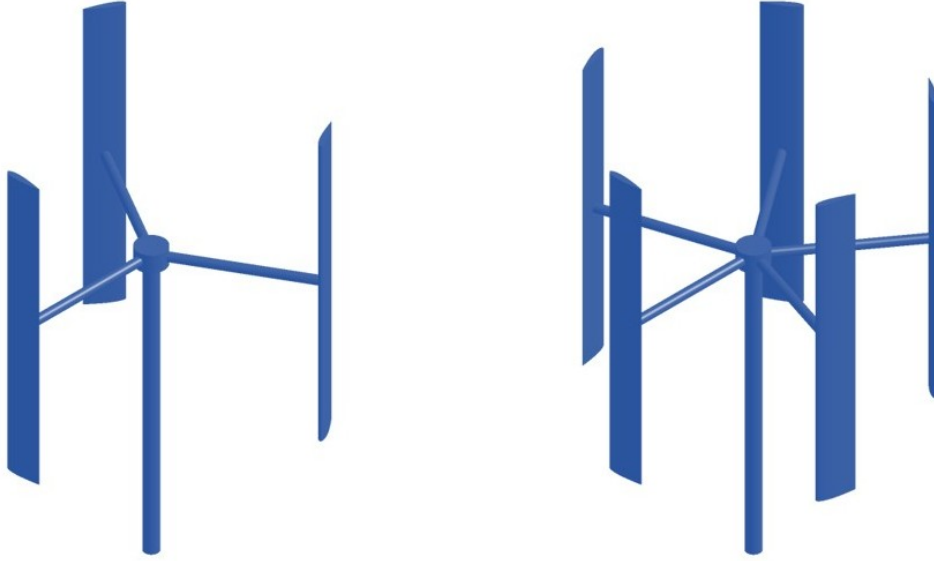


Figure 1: Representative models of three- and five-bladed rotors

During the whole rotational cycle, the blades of a VAWT experience strongly unsteady flow conditions. To illustrate the self-starting mechanism, consider a single non-pitching blade rotating counter-clockwise with angular velocity ω , as shown in Fig. 2. The instantaneous position of the blade is given by the azimuthal angle (θ), measured from the vertically upward direction. The vectorial addition of free-stream velocity (U_∞) and the tangential velocity ($R\omega$) form the effective velocity vector (U_{eff}) experienced by the blade. Here, R and ω denote the radius and angular speed of the turbine, respectively. The magnitude of U_{eff} and its effective instantaneous angle (α_{eff}) with the chord can be expressed as ([6–8]):

$$U_{eff} = U_\infty \sqrt{\lambda^2 + 2\lambda \cos \theta + 1}, \quad (1)$$

$$\alpha_{eff} = \tan^{-1} \left(\frac{\sin \theta}{\cos \theta + \lambda} \right). \quad (2)$$

where θ is measured positive in the anti-clockwise direction starting from the top position ($\theta = 0$), as illustrated in Fig. 2, and λ is the instantaneous tip-speed ratio, defined as:

$$\lambda = \frac{R\omega}{U_\infty}, \quad (3)$$

The geometric loading of the rotor is described by solidity (σ), which is defined by the following expression:

$$\sigma = \frac{Nc}{R}, \quad (4)$$

where N shows the number of blades in a rotor, and c is the chord-length of a blade.

At lower λ , ω (and the resultant tangential velocity of the blade) is small relative to U_∞ , so the relative flow is dominated by the free stream. As illustrated in Fig. 2, it yields a comparatively large α_{eff} and its large variations with time during a rotational cycle. As the rotor accelerates, the tangential velocity of a blade increases and contributes more strongly to the relative velocity, causing the relative

velocity vector to orient more toward the blade’s kinematics and progressively reducing α_{eff} . Consequently, the range of α_{eff} gets narrowed as λ increases, leading to a more stable aerodynamic response during the subsequent acceleration and steady operating stages. In the literature [9–11], the term self-starting was used with varying interpretations. In the present work, it is taken to refer to the ability of a turbine to accelerate autonomously from rest and reach a steady operating state in which the blade’s tip speed exceeds the wind speed. A VAWT is therefore considered to have self-started once it reaches $\lambda > 1$, at which point sustained rotation is established [12, 13].

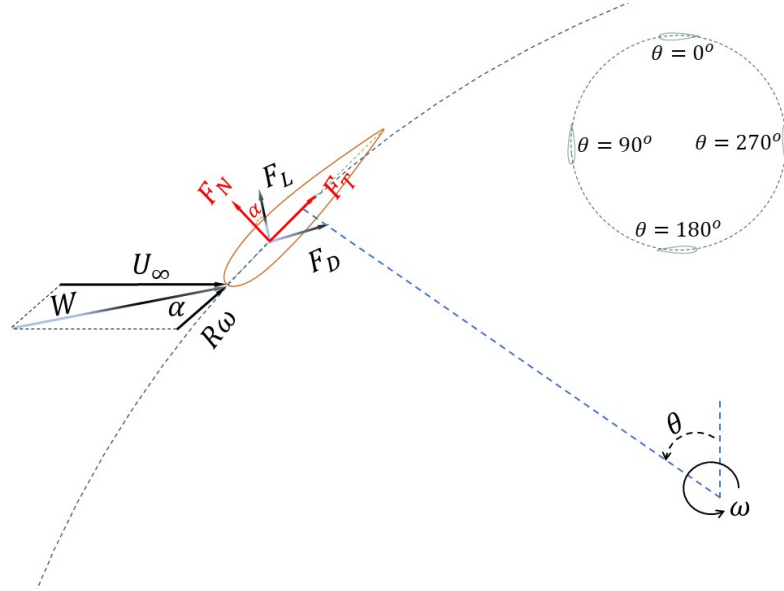


Figure 2: Characteristic velocities and forces acting on a blade in a VAWT

One important phenomenon associated with VAWTs that strongly influences their self-starting characteristics is dynamic stall. First reported in the context of helicopter aerodynamics [14], dynamic stall received substantial attention in the VAWT-related literature, because their start-up process frequently occurs in a low- λ regime, where the blades experience large, rapidly varying α_{eff} over the azimuthal cycle. The formation and shedding of large coherent flow structures cause intense unsteady aerodynamic loading on the blades. It can be detrimental to overall performance of the turbine and can also adversely affect its structural integrity by causing fatigue and triggering aeroelastic instabilities, *e.g.*, flutter, potentially leading to failure of the turbine’s components [15–17].

In the context of VAWTs, the initial operating stage, commonly termed the startup phase, occurs in low speed regimes (low- λ), where turbine geometry strongly governs the aerodynamic response. A key geometric parameter is σ , typically interpreted as the ratio of total blade planform area to the rotor’s swept area [18]. Prior work indicates that the self starting capability of Darrieus type VAWTs generally improves with increasing σ [19]. However, low- λ operation also places the turbine at an elevated risk of dynamic stall, motivating design and control strategies to mitigate stall induced losses and unsteady loading. For instance, variable pitching of blades was recommended in low- λ conditions by Sagharichi et al. [20], reporting a variable pitch turbine with $\sigma \approx 0.5$ operated in regimes prone to dynamic stall. Besides single-rotor VAWTs, experimental results for dual VAWT configurations showed that changes in the produced power could be weak at low λ , while lower σ increased sensitivity spacing between the rotors and skewness in the flow [21]. It implies that urban or array configurations should account for solidity, spacing, and skewed inflow effects. Complementing these findings, experimental data [22] for high- σ turbines ($\sigma \approx 0.42$ to 0.45) at low λ indicate that the startup regime is dominated by deep dynamic stall and strong unsteady loading, where accurate predictions may require two-dimensional modeling through unsteady Reynolds-Averaged Navier-Stoke Equations (URANs) augmented with simple correction factors to work with three-dimensional systems. Moreover, Tong et al. [23] reported that the chord-to-circumference ratio was an additional key design

parameter for small-bladed VAWTs rated below 10 kW. It reveals inherent trade offs between starting capability and power performance as the rotor’s diameter and chord length were varied. Collectively, these investigations indicate that geometric parameters, including the blade’s chord length, rotor’s diameter, and related quantities embedded within solidity-driven design, exhibit a strong influence on startup behavior and unsteady aerodynamics of VAWTs. However, significant gaps exist related to suitable geometric parameters for self-starting of VAWTs in the current literature. Our present work addresses this important aspect of designs of VAWTs, which systematically examines the influence of chord-length and number of blades, independent of solidity, to characterize their roles on the startup dynamics, dynamic stall, and the eventual steady-state λ . Therefore, the novelty of this work revolves around addressing the following important research questions that are unanswered in literature, according to the authors’ knowledge: (i) how does the turbines with different number of blades but with the same chord of each blade or same solidity of their rotors self start? (ii) what are the aerodynamic indicators for investigating the reasons behind their ability or inability to self start under different operating conditions? (iii) what is the role of flow unsteadiness in governing the onset of self-starting, dead-band behavior, and transition to sustained rotation in freely accelerating VAWTs? (iv) how do viscous effects, through their contribution to the aerodynamic moment, influence the self-starting process and limit or support the attainable operating state after startup?

To address these research questions, the present study examines how two geometric features, c and N , influence the start-up response of VAWTs. The motivation for this research work arises from the limited literature that explicitly couples variations in c and N . These are often discussed only through the solidity, even though solidity is primarily a geometric descriptor rather than a similarity parameter for the start-up dynamics [24]. The explanation of our work begins with describing the computational setup and geometric configurations in section 2. The results are presented in section 3 by systematically addressing the research questions posed earlier, beginning with a summary of the overall start-up outcomes and then relating the observed trends to the underlying aerodynamic mechanisms and their implications for both start-up and steady operating performance. Finally, the main conclusions are provided in Section 4.

2 Simulation Framework

We present the methodology adopted for the numerical simulations for flows around a range of configurations of VAWTs in this section, starting with the geometry and domain of the simulations (section 2.1), followed by explanation of the numerical solver (section 2.2). Then, we present the results of the mesh-convergence and time-step independence studies in section 2.3 with details of the validation cases in section 2.4.

2.1 Geometry of VAWTs and the Computational Domain

The primary geometric configuration of VAWTs considered in this study is inspired from the one used by Rainbird [25] in their experimental investigations. The other geometries are based on the same VAWT, as it was also extensively employed in other studies reported in recent literature [12, 26–29]. To investigate the influence of σ on the self-starting behavior of VAWTs, only c and N are varied, while R is kept constant for all configurations. Two configuration sets are considered, the equal-chord (EC) set and another equal-solidity (ES) set, as summarized in Table 1.

In the EC set, 3-bladed and 5-bladed configurations share identical chord lengths, such that the increasing N leads to higher σ . In the ES set, the chord of each blade of the 5-bladed configurations is reduced, such that their σ matches that of the corresponding 3-bladed system, isolating the effect of N at a fixed σ . This coordinated design enables the independent assessment of the roles of c , N , and σ on the self-starting behavior of the turbines.

Table 1: Geometric parameters of 3-bladed and 5-bladed VAWTs, where the subscripts for c and σ represent the corresponding number of blades in a turbines

Parameter	3 blades	5 blades
Set 1 c (mm) $c_3=c_5$	43, 63, 83, 103, 123	43, 63, 83, 103, 123
Set 2 c (mm) $\sigma_3=\sigma_5$	43, 63, 83, 103, 123	25.8, 37.8, 49.6, 61.6, 73.6
R (m)	0.375	0.375
H (m)	1	1
Blade profile	NACA0018	NACA0018
Moment of inertia (kg m ²)	0.018	0.018

To mitigate influence of boundaries of the computational domain on performance of the turbine and alleviate effects of blockage on the numerical results, we follow the practices recommended by Rezaeiha et al. [30]. The center of the turbine is placed at a distance of $10D$ from the inlet, top, and bottom boundaries, whereas the outlet is placed at a distance of $15D$.

2.2 Computational Method

This study employs OpenFOAM, an open-source finite-volume solver widely used for wind-turbine investigations ([31–35]). The incompressible unsteady Reynolds-averaged Navier–Stokes (URANS) equations (Eq. 6) for wind around the turbine are solved using a pressure-based, segregated algorithm. In this work, we use pimpleFoam, which merges PISO (Pressure Implicit Splitting of Operators) and SIMPLE (Semi-Implicit Method for Pressure-Linked Equations) into the PIMPLE procedure (outer SIMPLE-style loops with inner PISO-style correctors, [36]). PimpleFoam is expressly formulated as a large timestep-based transient solver for incompressible flows [37], relying on multiple outer corrections per timestep to maintain stability, accuracy, and efficiency of simulations for scenarios, such as flows over rotating VAWTs. Here, the spatial convective and diffusive terms are discretized using the second-order least-squares/linear gradients techniques, and the transient term is approximated via a second-order implicit scheme. The angular motion of a VAWT is handled via the sliding-mesh technique, which permits the rotor to rotate physically without requiring any re-meshing in the computational domain. Due to high-Reynolds number flows involved here, we model turbulence using the k – ω SST model augmented by the γ – Re_θ transition [38] to capture laminar–turbulent transition pertinent to situations encountered by VAWTs.

The incompressible URANS continuity and momentum equations solved in this work are

$$\nabla \cdot \bar{\mathbf{U}} = 0, \quad (5)$$

$$\rho \left(\frac{\partial \bar{\mathbf{U}}}{\partial t} + (\bar{\mathbf{U}} \cdot \nabla) \bar{\mathbf{U}} \right) = -\nabla \bar{p} + \nabla \cdot \left[(\mu + \mu_t) (\nabla \bar{\mathbf{U}} + (\nabla \bar{\mathbf{U}})^T) - \frac{2}{3} \rho k \mathbf{I} \right]. \quad (6)$$

Here, $\bar{\mathbf{U}}$ and \bar{p} are the Reynolds-averaged velocity and pressure, ρ is the fluid density, μ is the dynamic viscosity, μ_t is the eddy viscosity, k is the turbulent kinetic energy (appearing through the isotropic part of the Reynolds stresses), and \mathbf{I} is the identity tensor.

Turbulence closure is provided by the k – ω SST model, for which the transport equations are

$$\frac{\partial(\rho k)}{\partial t} + \nabla \cdot (\rho k \bar{\mathbf{U}}) = P_k - \beta^* \rho k \omega + \nabla \cdot [(\mu + \sigma_k \mu_t) \nabla k], \quad (7)$$

$$\frac{\partial(\rho \omega)}{\partial t} + \nabla \cdot (\rho \omega \bar{\mathbf{U}}) = \alpha \rho \frac{P_k}{k} - \beta \rho \omega^2 + \nabla \cdot [(\mu + \sigma_\omega \mu_t) \nabla \omega] + 2(1 - F_1) \rho \sigma_\omega \frac{1}{\omega} \nabla k \cdot \nabla \omega. \quad (8)$$

In Eqs. (7)–(8), k is the turbulent kinetic energy, ω is the specific dissipation rate, P_k is the production of k , and F_1 is the SST blending function.

2.3 Grid-Convergence and Timestep-Independence Tests

The computational domain around a turbine is discretized through unstructured, quad-dominant mesh, where a hierarchical refinement strategy is applied to obtain grid-independent solutions. The domain is partitioned into a static zone and a rotating zone with multiple refinement levels. In the static zone, the wake is refined as the refinement region 1 (RR1), extending to a downstream distance of $5D$ from the center of the turbine and to $2D$ in the vertical direction, as shown in Fig. 3(a). Within the rotating zone, we establish three refinements, including RR2 as the refinement in the core volume (see Fig. 3b), RR3 as an annular band along the trajectory of a blade (see Fig. 3c), and RR4 as an elliptical sheath enveloping each blade, with the enlarged view of the leading and trailing edges shown in Fig. 3d and Fig. 3f, respectively. Its overall extent is presented in Fig. 3e. To resolve the viscous sub-layers of the boundaries of the blades, inflated quadrilateral cells are introduced with a total of 20 layers of grid cells from the wall, as suggested by Ramirez and Saravia [39]. The first-cell height is chosen based on the value of y^+ as 5 stretching the grid with a ratio of 1.08, following the recommendation by Li et al. [40].

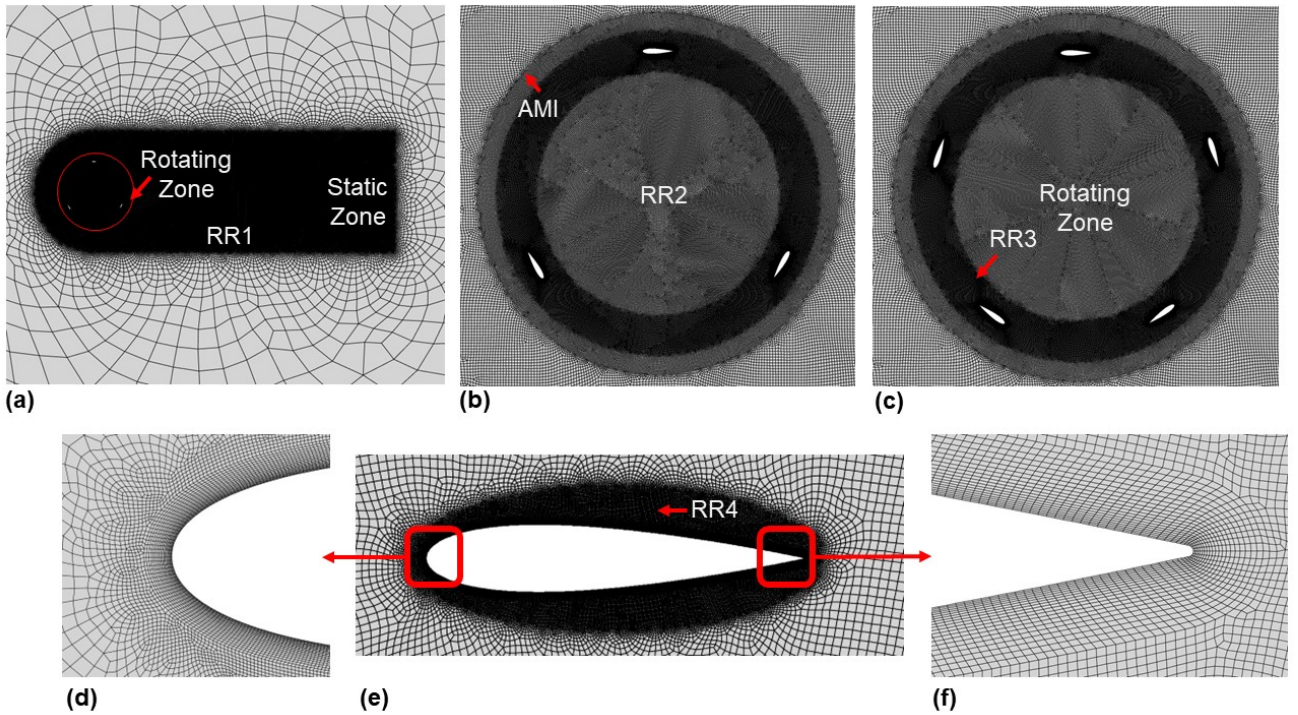


Figure 3: Nested refinement regions inside the static and rotating zones (RR1–RR4)

We carry out the grid-convergence and timestep-independence tests on a 3-bladed turbine with an inlet velocity of 8 m/s, where the rotor’s moment of inertia is kept at 0.018 kg m^2 , following the benchmark configuration reported by Rainbird [25]. Three meshes with coarse, medium, and fine resolutions are generated for the grid-independence study, and the cell sizes in RR1 to RR4 are varied systematically, as shown in Table 2. Figure 4 presents the tip-speed ratios versus time, obtained using the three mesh configurations to compare the self-starting behavior of the turbine. It is evident that the medium and fine grids exhibit nearly identical behavior and converge to the same steady state λ . , following the practices reported by Asr et al. [26] and Khalid et al. [12], t^* denotes the total time normalized by the time required for the turbine to reach its steady-state λ here.

A time-step independence study is essential to ensure the numerical accuracy and reliability of transient simulations. In unsteady problems, such as the self-starting process of VAWTs, the time-step size directly influences how well the solver can resolve rapid variations in aerodynamic forces, moments, and flow structures around the blades. In this work, we select three timestep sizes, including $\Delta t_1 = 0.0005 \text{ s}$, $\Delta t_2 = 0.0001 \text{ s}$, and $\Delta t_3 = 0.00005 \text{ s}$. We find that the tip-speed ratio of the VAWT for

Table 2: Refinement sizes in each region and total cell counts.

Refinement Level	RR1 (m) $\times 10^{-3}$	RR2 (m) $\times 10^{-3}$	RR3 (m) $\times 10^{-3}$	RR4 (m) $\times 10^{-4}$	No. of cells
Coarse	9	7	5	3.5	163,000
Medium	7.5	3.5	2	2.5	312,000
Fine	6	2	1.5	2	540,000

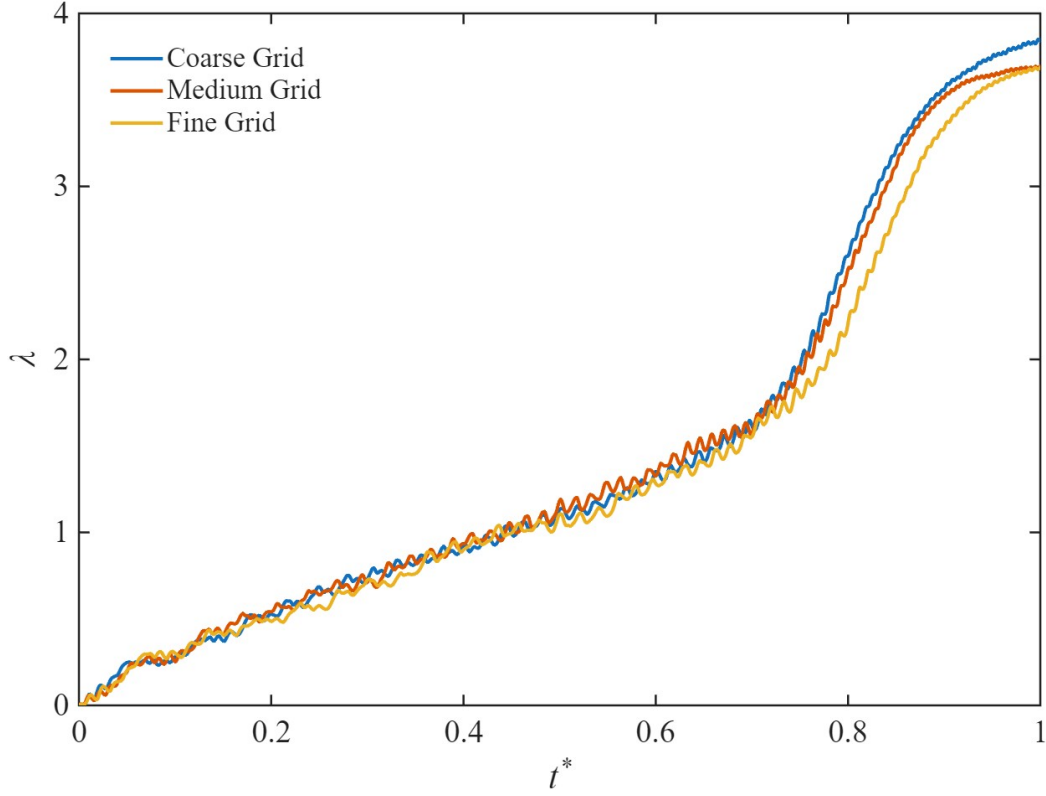


Figure 4: Comparison of tip-speed ratios of a VAWT using three different grids

Δt_2 and Δt_3 settles at a λ that does not have a significant difference, as shown in Fig. 5, the former reaching steady-state λ of 2.77 and the latter at 2.62. Despite the small difference, Δt_3 is still selected for all subsequent simulations to provide greater temporal resolution and confidence in the results.

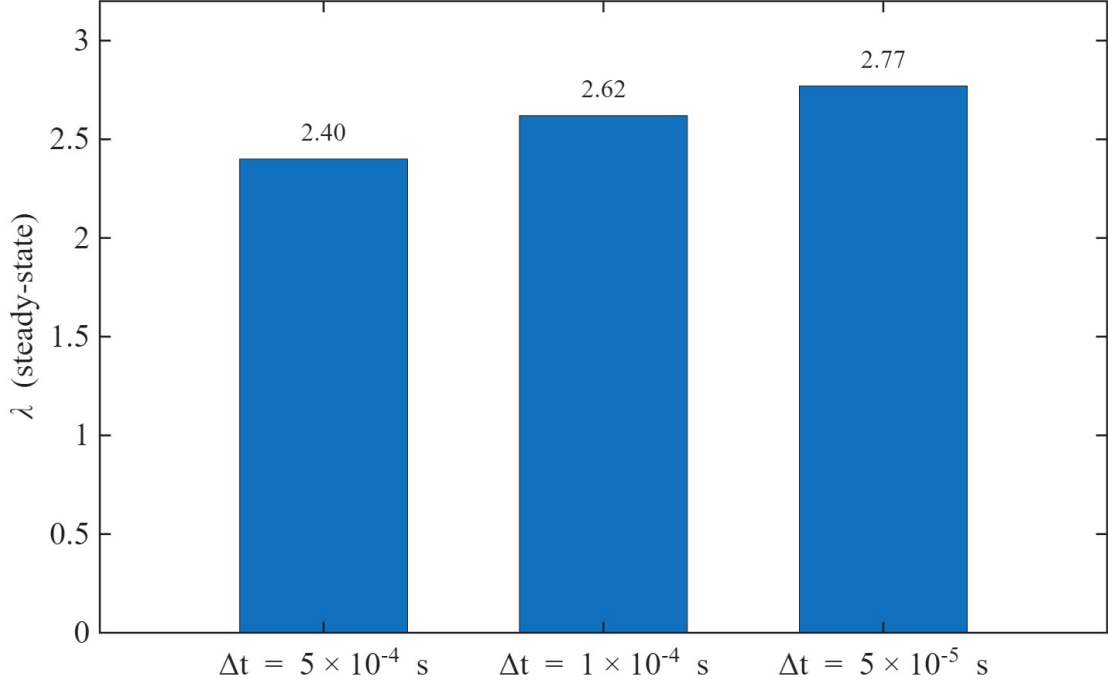


Figure 5: Comparison of the steady-state λ 's for three timestep sizes

2.4 Validation

Now, we validate our computational framework using the experimental data provided by Rainbird [25] and the numerical results of Khalid et al. [12] and Asr et al. [26]. The VAWT geometry used in these studies consists of a 3-bladed turbine with $c = 83$ mm, $R = 0.375$ m, and $J = 0.018$ kgm², subjected to a wind speed of 6 m/s. As shown in Fig. 6, the four stages of the VAWT's self-starting process, described by Du et al. [41], are clearly captured. These stages include an initial nearly-linear acceleration, a plateau with only a slow increase in λ , a rapid-acceleration phase, and finally convergence to a quasi-steady operating λ . The comparison indicates very good agreement of our presently obtained results with the experimental data while remaining consistent with previously reported simulations. The experiment employs a finite-span rotor and includes resistive torques from the test rig and drivetrain, whereas our present two-dimensional CFD assumes an infinite span and a freely rotating turbine without structural or generator damping. Although such idealizations are known to be mildly over-predictive relative to experiments, the close correspondence of our curves with Rainbird [25] and their alignment with the results from Khalid et al. [12] and Asr et al. [26], provide confidence in our computational setup and supports the subsequent analysis of self-starting behavior of VAWTs in this work.

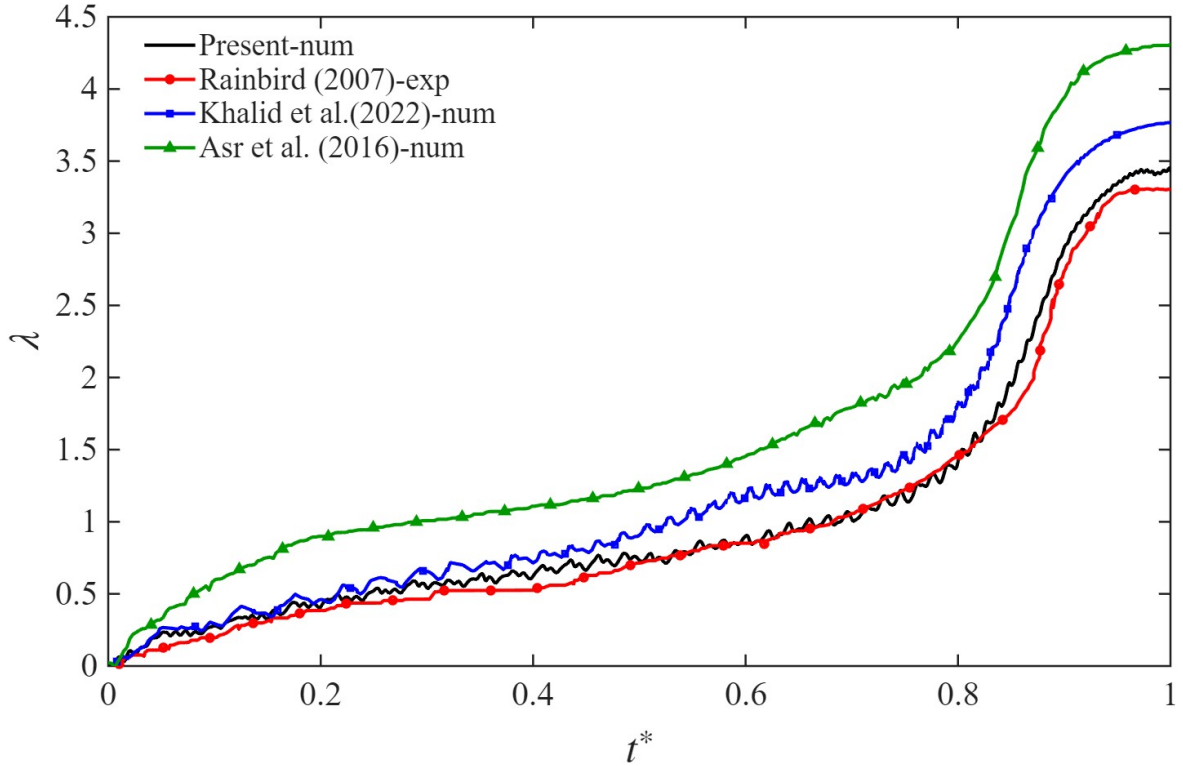


Figure 6: Comparison of λ obtained from our computational simulation with experimental data of Rainbird [25] and numerical results from Khalid et al. [12] and Asr et al. [26]

3 Results and Discussion

The results from our investigations are organized around the two configuration sets, including the EC set and the ES set introduced in Section 2.1. Within each set, comparisons are made between the 3-bladed and 5-bladed turbines to isolate the effect of the number of blades N . In the EC set, the turbine with 3 blades establish the reference trend in λ_{steady} at lower σ , while the 5-bladed VAWT isolate the effect of the increasing N at a fixed c , which results in higher σ . In the ES set, the chord of a blade for the 5-bladed turbine is reduced to match the solidity of the corresponding 3-bladed turbine, isolating the effect of N at a constant σ . Together, these comparisons enable a systematic assessment of how c , N , and σ influence the self-starting torque, transient acceleration, and λ_{steady} of VAWTs at inflow velocities of 4 m/s, 6 m/s, and 8 m/s.

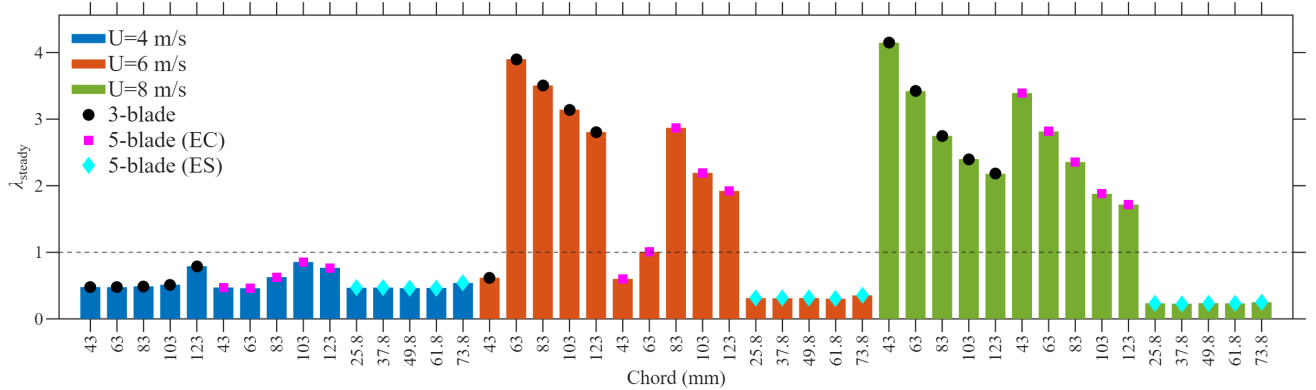


Figure 7: Bar chart summarizing λ_{steady} , versus c for the EC and ES 3- and 5-bladed configurations at $U_{\infty} = 4, 6, \text{ and } 8 \text{ m s}^{-1}$ with the dashed line representing $\lambda_{\text{steady}} = 1$

Figure 7 exhibits λ_{steady} as a function of the chord of a blade for all configurations under the aforementioned flow conditions. For the 3-bladed configurations, λ_{steady} increases significantly with the inflow velocity for all chord lengths. At the velocity of 4 m/s, all cases demonstrate $\lambda_{\text{steady}} < 1$ and therefore do not self-start. At $U_{\infty} = 6$ m/s, λ_{steady} increases sharply, reaching values above 3 for intermediate chord lengths and decreasing slightly for the larger chord-lengths. For $U_{\infty} = 8$ m/s, the 3-bladed turbine attains the highest λ_{steady} , with its clear monotonic decrement as the chord of a blade increases from 43 mm to 123 mm. For the 5-bladed turbines in the EC configurations, λ_{steady} is consistently lower than for the corresponding 3-bladed counterparts at the same chord of each blade and the inflow velocity. For $U_{\infty} = 4$ m/s, λ_{steady} of all the cases considered here remains below unity and, therefore, do not self-start. At $U_{\infty} = 6$ m/s, self-starting of turbines occurs only for the intermediate chords, and λ_{steady} remains below the corresponding values for the 3-bladed VAWTs. For $U_{\infty} = 8$ m/s, the configuration in the EC set exhibit moderate λ_{steady} that decreases with an increasing chord of a blade. For the 5-bladed ES configurations, λ_{steady} remains low for all inflow velocities and chord lengths. Even at $U_{\infty} = 8$ m/s, λ_{steady} does not exceed approximately 0.4, and none of the turbines in this set exhibits self starting behavior. Overall, Fig. 7 shows that increasing N at a fixed c reduces λ_{steady} , while increasing N at a fixed σ leads to a stronger suppression of self-starting and sustained rotation. The highest λ_{steady} occurs for the 3-bladed configurations at the lowest σ and highest inflow velocity.

Figure 7 also reveals the existence of a critical chord length (c_{crit}) for each configuration. It is clear that the only turbines with $c \geq c_{\text{crit}}$ are able to self start and overcome the dead band to show self starting. Therefore, the value of c_{crit} represents the minimum c required for self starting of a VAWT for a given N , R , and J . It also corresponds to the chord that maximizes λ_{steady} within each configuration family, indicating a trade off between startup capability and steady state performance. These trends are also observed from the temporal profiles of λ presented in Figs. 8 to 13. Please note that the aim here is not to determine c_{crit} precisely in this study, but providing a good estimates of the range of the geometric characteristics of a VAWT capable of self starting, as summarized in Table 3.

Table 3: Ranges for c_{crit} separating non-self-starting ($\lambda_{\text{steady}} < 1$) and self-starting ($\lambda_{\text{steady}} > 1$) regimes

U_{∞} (m/s)	3 blades	5 blades (EC)	5 blades (ES)
4	$c_{\text{crit}} > 123$ mm	$103 < c_{\text{crit}} < 123$ mm	$c_{\text{crit}} > 73.8$ mm
6	$43 < c_{\text{crit}} < 63$ mm	$63 < c_{\text{crit}} < 83$ mm	$c_{\text{crit}} > 73.8$ mm
8	$c_{\text{crit}} < 43$ mm	$c_{\text{crit}} < 43$ mm	$c_{\text{crit}} > 73.8$ mm

Next, Figs. 8, 9, and 10 present the time histories of λ for the 3-bladed and 5-bladed turbines in the EC configuration at $U_{\infty} = 4$ m/s, 6 m/s, and 8 m/s, respectively. For all the three inflow velocities, the 5-bladed turbine accelerates more rapidly from rest and reaches its steady state earlier than the 3-bladed turbine, indicating a shorter startup time. However, λ_{steady} attained by the 5-bladed turbine is consistently lower than that of the 3-bladed turbine. It demonstrates that increasing the number of blades enhances the initial aerodynamic torque but penalizes the long term rotational performance. Across the EC and ES configurations, the present results show that the effect of N on self-starting is strongly conditioned by how the geometry is modified. In the EC set (same c), increasing N from 3 to 5 generally promotes a faster initial rise in λ and a shorter startup period, particularly at $U_{\infty} = 6$ and 8 m/s, but it also leads to a lower λ_{steady} after startup. In contrast, in the ES set (same σ), the reduction in c required for the 5-bladed turbine suppresses blade-level aerodynamic loading, and the 5-bladed cases remain trapped in the dead-band (non-self-starting) over the range considered, even when the corresponding 3-bladed cases self-start. These observations indicate that increasing the number of blades alone does not guarantee improved self-starting. Rather, its influence depends on the associated scaling of c and the resulting unsteady aerodynamic response. It is broadly consistent with Sun et al. [42] in the sense that effects of N are wind-speed dependent and can influence startup time but differs

in the final outcome. It is because Sun et al. [42] considered turbines with an offsetting pitching angle (which can delay or suppress adverse vortex development), whereas the present work isolates fixed-pitch geometric effects in freely accelerating VAWTs. As a result, the present simulations highlight a startup–performance trade-off: a higher blade count may assist early acceleration under equal- c conditions, yet it can reduce the attainable steady operating state and, under equal- σ chord reduction, inhibit self-starting altogether.

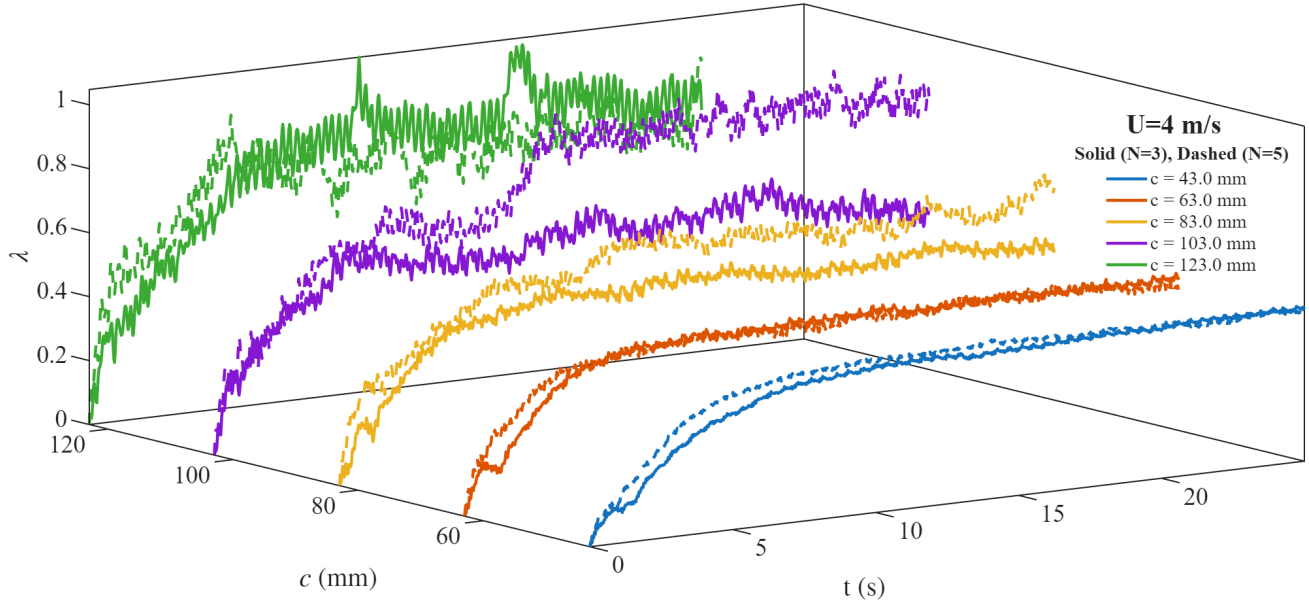


Figure 8: Comparative time history of λ for the 3 and 5 blade turbines in the EC configuration at $U_\infty = 4$ m/s.

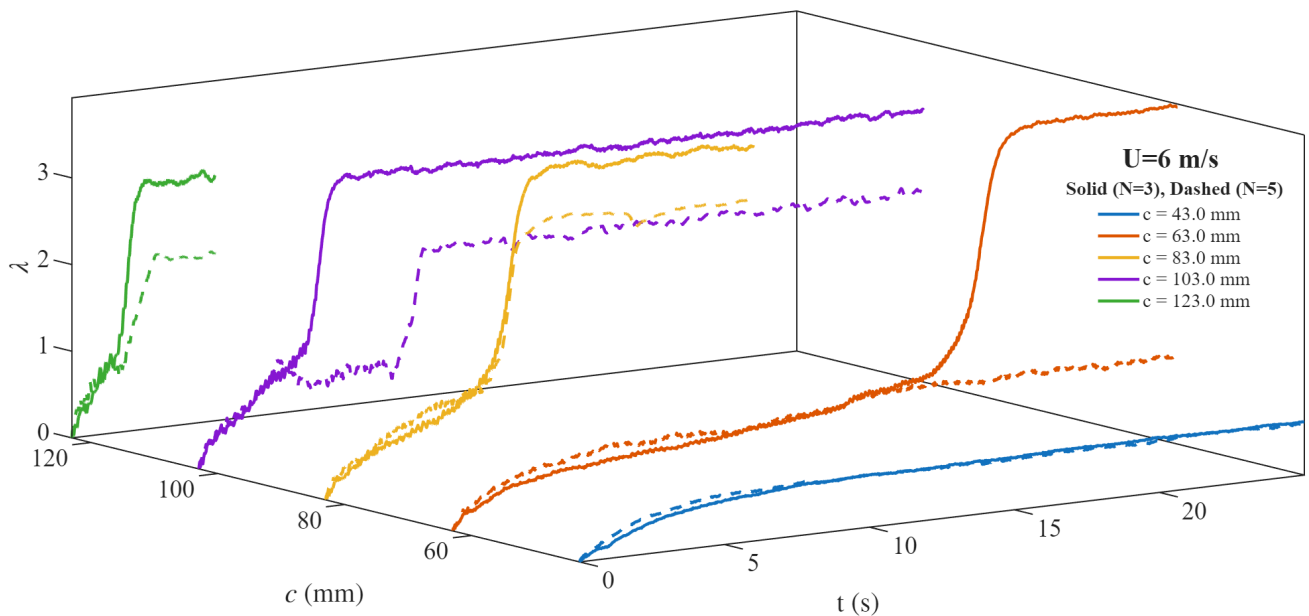


Figure 9: Comparative time history of λ for the 3 and 5 blade turbines in the EC configuration at $U_\infty = 6$ m/s.

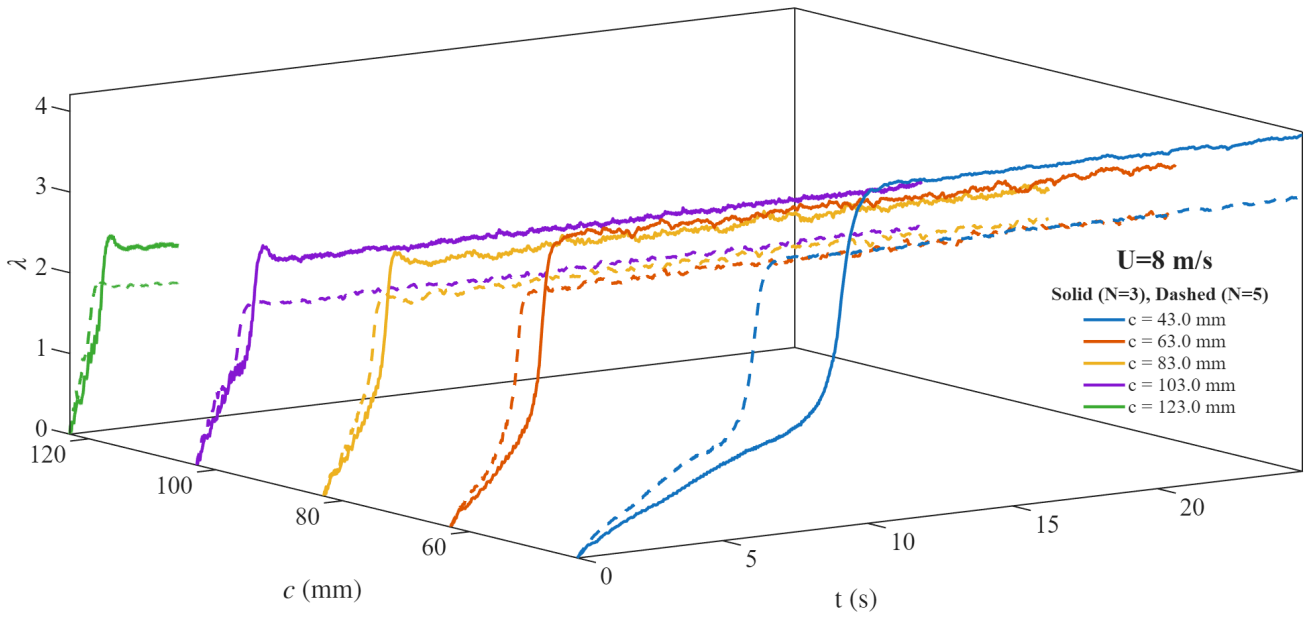


Figure 10: Comparative time history of λ for the 3 and 5 blade turbines in the EC configuration at $U_\infty = 8$ m/s.

Figures. 11, 12, and 13 show the corresponding time histories for of the turbines, belonging to the ES configuration at $U_\infty = 4$ m/s, 6 m/s, and 8 m/s, respectively. The 5-bladed turbine does not achieve self starting for any of the inflow velocities considered here. It is found that λ remains low and increases only gradually with time, indicating that the turbine remains trapped in the dead band and does not reach a sustained rotational state. Contrarily, the 3-bladed turbine is able to self start and reach a steady λ . It demonstrates that, for the ES family of VAWTs, increasing the blade number inhibits self starting rather than promoting it.

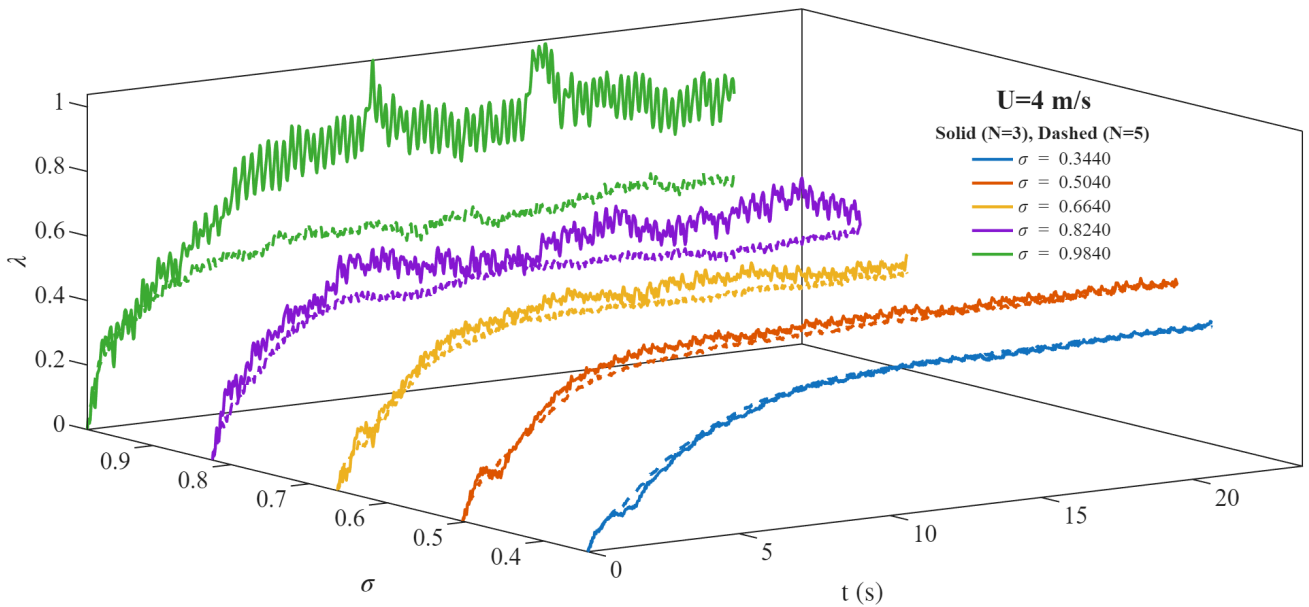


Figure 11: Comparative time history of λ for the 3 and 5 blade turbines in the ES configuration at $U_\infty = 4$ m/s.

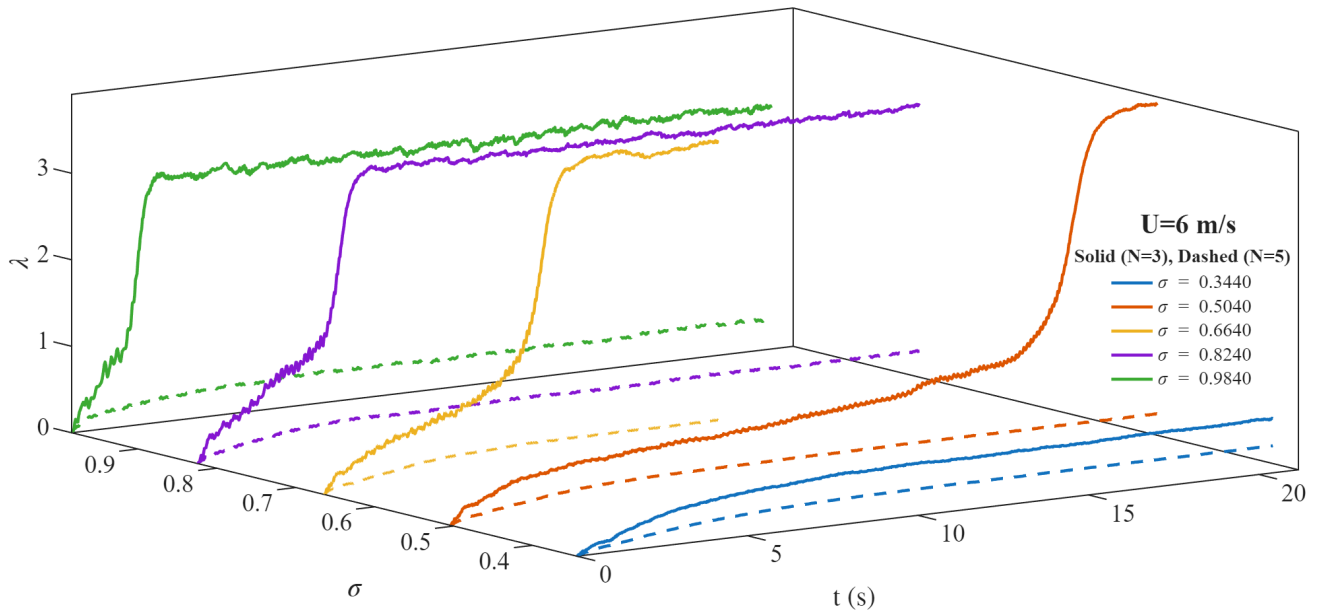


Figure 12: Comparative time history of λ for the 3 and 5 blade turbines in the ES configuration at $U_\infty = 6$ m/s.

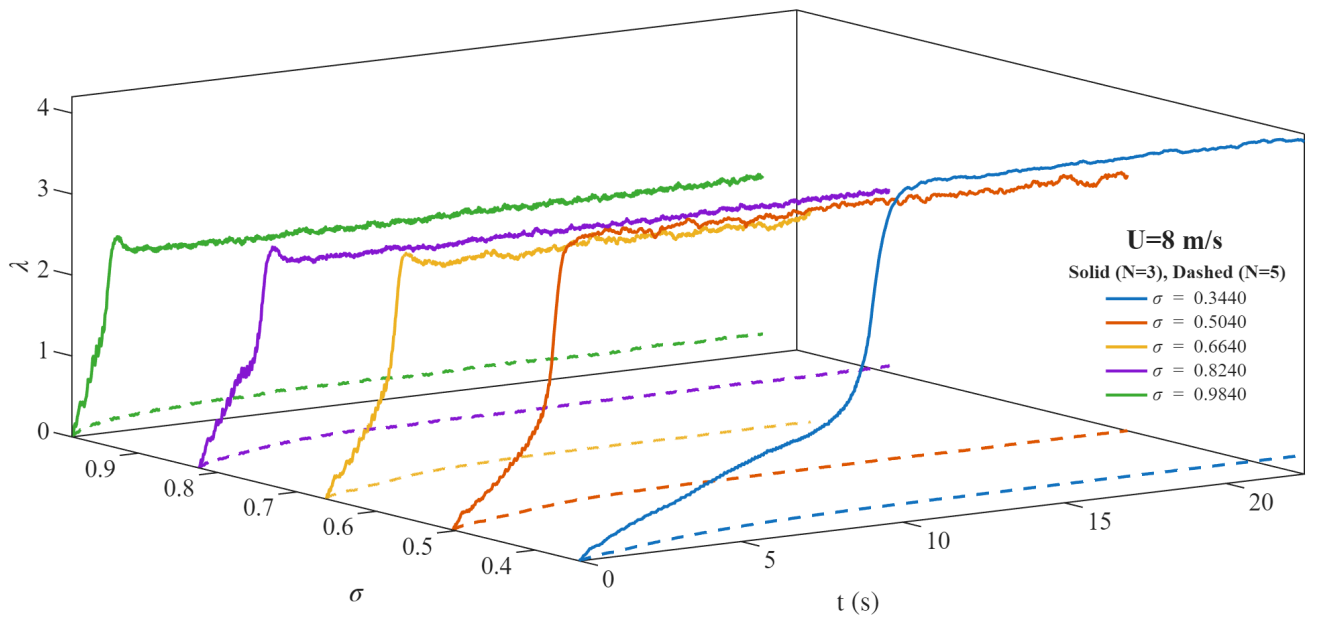


Figure 13: Comparative time history of λ for the 3 and 5 blade turbines in the ES configuration at $U_\infty = 8$ m/s.

3.1 Dynamic Stall and Blade–Vortex Interaction

In this subsection, the development of vortical structures, blade–vortex interactions (BVI), and their influence on both the startup process and the steady-state behavior are examined. Particular attention is paid to the role of dynamic stall in shaping the unsteady aerodynamic loads experienced by the blades and production of the overall torque by the turbines.

Dynamic stall is generally considered to occur on an airfoil or a lifting surface when it is subjected to time-dependent oscillatory motion, such that the effective angle-of-attack (α_{eff}), exceeds the corresponding static stall angle, (α_{ss}) [43, 44]. This phenomenon is inherently unsteady and depends not only on the instantaneous value of α_{eff} , but also on its rate of change and on the kinematics of the surface. Consequently, the distinction between static and dynamic stall is closely related to the rate of

change of angle-of-attack ($\dot{\alpha}$). However, no universal quantitative definition exists that uniquely separates static and dynamic stall based on $\dot{\alpha}$ alone [45]. Instead, dynamic stall is commonly characterized using non-dimensional parameters that reflect the level of flow unsteadiness. One such parameter that measures the degree of unsteadiness in the flow is the reduced frequency (k) [46], which is defined with respect to θ as:

$$k_{\theta} = \frac{\omega c}{2U_{\text{eff}}}, \quad (9)$$

This parameter was originally introduced for aerodynamics of rotors of helicopters but is also applicable to VAWTs, where it provides a measure of the unsteadiness associated with the azimuthal rate of change of the blade. More directly relevant to dynamic stall in VAWTs is the reduced frequency associated with pitching motion [47] which is defined below:

$$k_{\alpha} = \frac{\dot{\alpha}_{\text{eff}} c}{2U_{\text{eff}}}, \quad (10)$$

As noted by Leishman [46], dynamic stall may arise once k enters the unsteady regime. When $k = 0$, the flow is steady, implying no lag in the response of the surrounding fluid to the blade kinematics. For $0 \leq k < 0.05$, the flow may be regarded as quasi-steady, and unsteady effects are generally weak and often negligible. In contrast, for $k \geq 0.05$, the flow becomes increasingly unsteady, and dynamic stall effects may become significant.

From a physical standpoint, this unsteadiness can be interpreted as a delay in the response of the surrounding flow field to the blade's motion. When its kinematics vary sufficiently rapidly, the flow is unable to adjust instantaneously to the imposed motion. This delayed response causes flow reversal within the boundary layer, initiating near the trailing edge and progressively moving upstream once α_{eff} exceeds α_{ss} . As the upstream influence of this reversed flow reaches the leading edge, the separated shear layer rolls up into a concentrated leading-edge vortex, commonly referred to as the dynamic stall vortex (DSV). As the DSV convects downstream over the suction surface, it induces a transient increase in lift. Its continued convection and interaction with oppositely signed vorticity ultimately destabilize the vortex, leading to its detachment and a sharp drop in the moment coefficient. Afterwards, the flow progresses toward a fully separated state until reattachment occurs at a lower α .

In the context of VAWTs, the recent experimental work of Le Fouest and Mulleners [47] is particularly relevant, as they quantified the delay in the aerodynamic response using a single blade subjected to prescribed rotation and distinguished between deep stall, light stall, and no-stall regimes. Deep stall corresponded to cases in which the dynamic stall vortex had sufficient time to develop fully before detaching, leading to strong unsteady loads, whereas light stall occurred when the blade reached its maximum α_{eff} before the vortex was fully formed, resulting in a weaker unsteady loading. The no-stall regime was associated with conditions under which α_{eff} did not exceed α_{ss} , which in their study corresponded to operations at large λ 's. This approach of quantifying the dynamic-stall regimes is not directly applicable in our present work. The experiments done by Le Fouest and Mulleners [47] were based on a single-blade geometry with predefined rotations, which is rather a simple scenario. Our present simulations consider the collective passive aerodynamic response of the VAWTs composed of multiple blades. Consequently, it is difficult to clearly identify the instant at which an individual blade exceeds its static stall angle, or the corresponding instant at which the pitching moment coefficient reaches its maximum value, which are required to compute the delay in the response. Instead, we examine the unsteady behaviour using the temporal histories of instantaneous θ , α_{eff} , λ , k_{α} and k_{θ} , which provide qualitative and comparative insights for the presence and nature of dynamic stall under different operating conditions.

To investigate the role of dynamic stall in the self-starting process, a representative 3-bladed VAWT exhibiting self-starting behavior is selected for the detailed analysis. The instantaneous evolution of the kinematic quantities introduced earlier, together with the associated vorticity fields for the case with

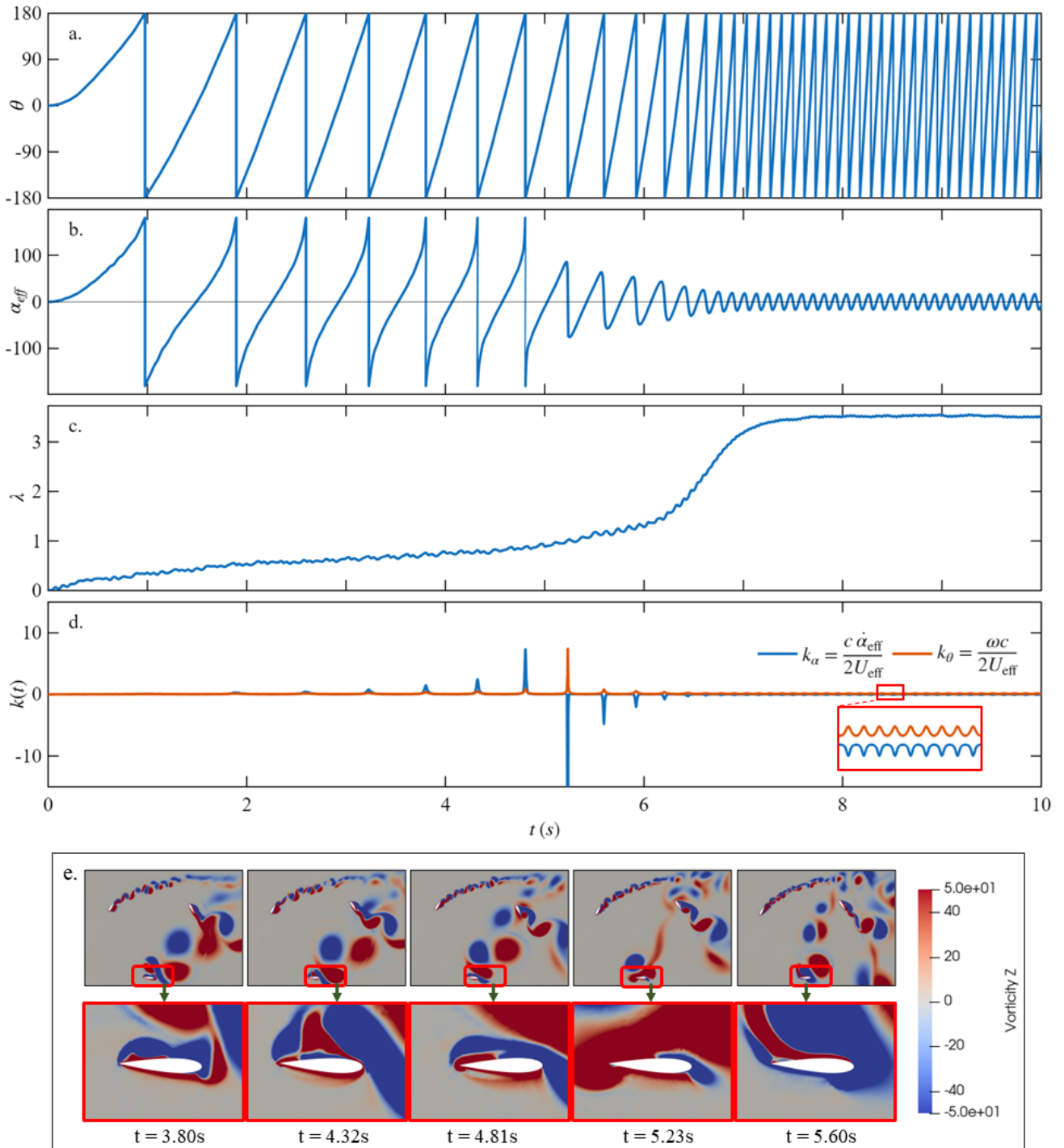


Figure 14: Single-blade kinematic time histories for a self-starting case with $N = 3$, $c = 83$ mm, and $U_\infty = 6$ m/s. Shown are (a) azimuthal position $\theta(t)$, (b) effective angle of attack $\alpha_{\text{eff}}(t)$, (c) tip-speed ratio $\lambda(t)$, (d) reduced frequencies $k_\alpha(t)$ and $k_\theta(t)$, and (e) Vorticity Fields at specified instants figure changed to add the zoomed in section

$U_\infty = 6$ m/s and $c = 83$ mm, is presented in Fig. 14. The corresponding self-starting 5-bladed turbines exhibit qualitatively similar kinematic and flow features, therefore, only the 3-bladed configuration is discussed here for brevity, without loss of generality. From Fig. 14a, the evolution of the azimuthal position illustrates how the rotational speed increases with time, while Fig. 14c shows that, in the initial phase of the process, the turbine operates at very low values of λ . Figure 14b presents evidently that α_{eff} experiences very large excursions at the beginning of the rotation, well beyond typical static stall angles, which were reported in literature to lie approximately between 13° and 20° for NACA0018 depending on Reynolds number [45, 48–50]. However, large excursions of α_{eff} alone are not sufficient to infer the onset of dynamic stall, since the existence, strength, and influence of dynamic stall depend on the unsteady time scale of a blade's motion. The reduced frequency provides a measure to quantify these effects. The unsteadiness in the flow becomes more pronounced at approximately $t \approx 1.8$ s, where a noticeable change in the reduced frequencies is observed. At this time instant, a small spike appears in Fig. 14d, which coincides with the blade reaching $\theta \approx 180^\circ$. Similar spikes are observed in successive cycles at the same azimuthal position, with gradually increasing magnitude. At $t \approx 4.81$ s, a sharp increase in k_α is observed, indicating a very rapid change in α_{eff} over a short time interval. A similar but comparatively smaller increase is also observed in k_θ . As shown in Fig. 14d, both reduced frequencies attain their maximum excursions at $t \approx 5.2$ s. At this instant, k_θ exhibits a sharp positive spike, whereas k_α undergoes a very large negative spike, indicating an abrupt change in the blade kinematics with the blade passing through $\theta \approx 180^\circ$, where U_{eff} becomes small. Following this event, the magnitudes of both reduced frequencies decrease rapidly and only small fluctuations remain, while the turbine subsequently accelerates, and λ increases toward its steady value, as shown in Fig. 14c.

Following the experimental observations of Hill et al. [51] and Du et al. [41], the self-starting process in the present case can be segmented into four distinct phases. The initial startup phase occurs for $0 < t < 1.9$ s, where $t = 1.9$ s corresponds to the time at which the first small surge in the reduced frequencies is observed, while only a nearly linear increase in λ is present. The plateau stage, commonly referred to as the dead-band, extends from $1.9 < t < 5.2$ s. The time $t = 5.2$ s corresponds to the instant at which the largest positive peaks in both reduced frequencies are observed. During this interval, λ remains largely unchanged, as shown in Fig. 14c, indicating that the turbine experiences only a very gradual increase in its angular velocity despite the presence of intermittent unsteady events. It is followed by a rapid acceleration phase for $5.2 < t < 6.62$ s, during which the turbine undergoes runaway acceleration and λ increases sharply. Finally, a steady operating phase is reached for $t > 6.62$ s. The steady operating phase is defined here as the regime in which $\alpha_{\text{eff}}(t)$ exhibits a sinusoidal profile with the rotational cycle of the turbine, and both reduced frequencies exhibit a stable, quasi-periodic pattern as shown in the magnified inset of Fig. 14d.

Now, Fig. 14e presents the vorticity fields at the instants corresponding to the spikes observed in the reduced frequencies. At $\theta = 180^\circ$, the suction side of the blade transitions from the inward half of the trajectory to the outward half, a position at which the interaction between oppositely signed vorticity shear layers becomes particularly pronounced. During the first half of the rotation ($\theta = 0^\circ$ to 180°), the blade's angle-of-attack exceeds α_{ss} , initiating boundary-layer flow reversal that develops from the trailing edge and progressively advances upstream. This reverse flow displaces the positive-vorticity shear layer associated with the inward side of the blade. By the time the blade reaches $\theta = 180^\circ$ at $t = 3.8$ s (the selected instant at which a second peak in k_θ and k_α is observed) the flow is largely separated, consistent with the strong spikes in the reduced frequency observed at this azimuthal position (see Fig. 14d). As the turbine continues to accelerate, and its ω increases from cycle to cycle, the extent of boundary-layer separation is progressively reduced for $t > 5.23$ s as seen in Fig. 14e. The contour plots of vorticity in Fig. 14e clearly shows that the displaced positive-vorticity shear layer is observed to recover and migrate back toward the blade on the inward half of the trajectory in successive cycles. This recovery coincides with the growth and subsequent decay of the reduced-frequency spikes, indicating a gradual stabilisation of the near-blade flow as λ increases.

For the turbines with 3 and 5 blades that do not self-start, the temporal histories of θ , α_{eff} , λ ,

and the reduced frequencies are shown in Fig. 15. Both types of turbines remain trapped within the dead-band regime, with λ remaining below unity during the whole time. Although brief excursions of k_α and k_θ above the quasi-steady threshold are observed, with peak values reaching approximately 0.1 – 0.2, these events are intermittent and do not persist over consecutive cycles. Importantly, they are not accompanied by any sustained increase in λ , indicating that these localized unsteady events are insufficient to reorganize the near-blade flow in a manner that produces net positive torque and runaway acceleration. It is important to note that all simulations in our present work are run for a sufficiently long physical time to ensure that the observed behaviour is not a transient artifact of the initial conditions. Particularly, the non-self-starting cases are run for more than 25 s of physical time, consistent with startup durations commonly adopted in the literature [29], and no delayed transition to self-starting is observed. Over this duration, the flow remains strongly separated for most of the cycle, with only limited intervals when $\alpha_{\text{eff}} < \alpha_{\text{ss}}$. This observation confirms that the absence of self-starting in these cases is a persistent dynamical outcome rather than a delayed transient response.

Further analysis of temporal profiles of the reduced frequencies in Fig. 14d and boundary layer transition in Fig. 14e reveal the physical origin of the two-stage sequence preceding self-starting. In the first stage at $t \approx 4.8$ s (see Fig. 14e), a pronounced peak appears in k_α alone. Since k_α scales with $\dot{\alpha}_{\text{eff}}/U_{\text{eff}}$, this initial peak is primarily driven by a rapid change in α_{eff} over a short time interval, indicating a sudden reorientation of the relative inflow perceived by the blade. It corresponds to a kinematic event in which the blade transitions rapidly between flow states, producing a large $\dot{\alpha}_{\text{eff}}$ even though the azimuthal motion remains comparatively slow. In the subsequent cycle at $t \approx 5.23$ s, as shown in Fig. 14e, a second peak occurs in k_α now accompanied by a concurrent peak in k_θ . This second event reflects the combined effect of a rapid change in α_{eff} and a strong kinematic amplification associated with the azimuthal motion, occurring at an instant when U_{eff} becomes small. The simultaneous amplification of both reduced frequencies marks a regime in which the blade motion and the flow response are strongly coupled, and it coincides with the onset of a rapid increase in λ for the turbine to fully self-start. These processes do not occur for turbines incapable of self-starting, although α_{eff} may undergo large excursions, its associated rates of change and kinematic amplification do not simultaneously undergo their respective peaks in k_α and k_θ that appears to be required for causing a large acceleration of a turbine to take it to a steady λ .

To further explain the unsteady fluid dynamics, experimental particle-image velocimetry (PIV) based research for single-bladed turbines, undergoing prescribed rotations [47, 52], showed that the DSV around the blade followed a relatively repeatable sequence. Once α_{eff} exceeds α_{ss} , flow reversal initiates within the boundary layer, and the separated leading-edge shear layer rolls up to form a DSV at moderate azimuthal positions, typically around $\theta \approx 30^\circ$ to 40° . Continued shear-layer feeding allows the vortex to grow in size and strength while convecting along the suction side of the blade, producing a sharp rise in unsteady aerodynamic loading. As the event progresses, an oppositely signed vorticity layer develops between the blade's surface and the vortex that interrupts the feeding process and cause the vortex to detach from the blade near $\theta \approx 140^\circ$ to 160° . Following this detachment, the associated loss of suction produces a sharp drop in the pitching moment coefficient C_m [46, 47]. Due to the prescribed kinematics of the blade, these processes are repeatable from cycle to cycle and are commonly reported using phase-averaged flow fields. In the present simulation framework, the turbine rotates freely in a continuously accelerating regime with a time-varying λ . Here, all the blades are modeled to constitute a single rotating turbine. This computational process does not allow the computation of aerodynamic forces and moments for an individual blade. Therefore, a conventional moment-based dynamic stall analysis for a single blade is not possible here. It means that we need to rely on the kinematic analysis for an individual blade during the self-starting process to examine its unsteady aerodynamic behavior associated with dynamic stall. This explanation provides the justification for our analysis more focused on kinematics of an individual blade, using α_{eff} in our earlier discussion. Dynamic stall behavior is examined only during intervals in which the level of unsteadiness is sufficiently high to support the formation and evolution of coherent dynamic-stall flow structures. As

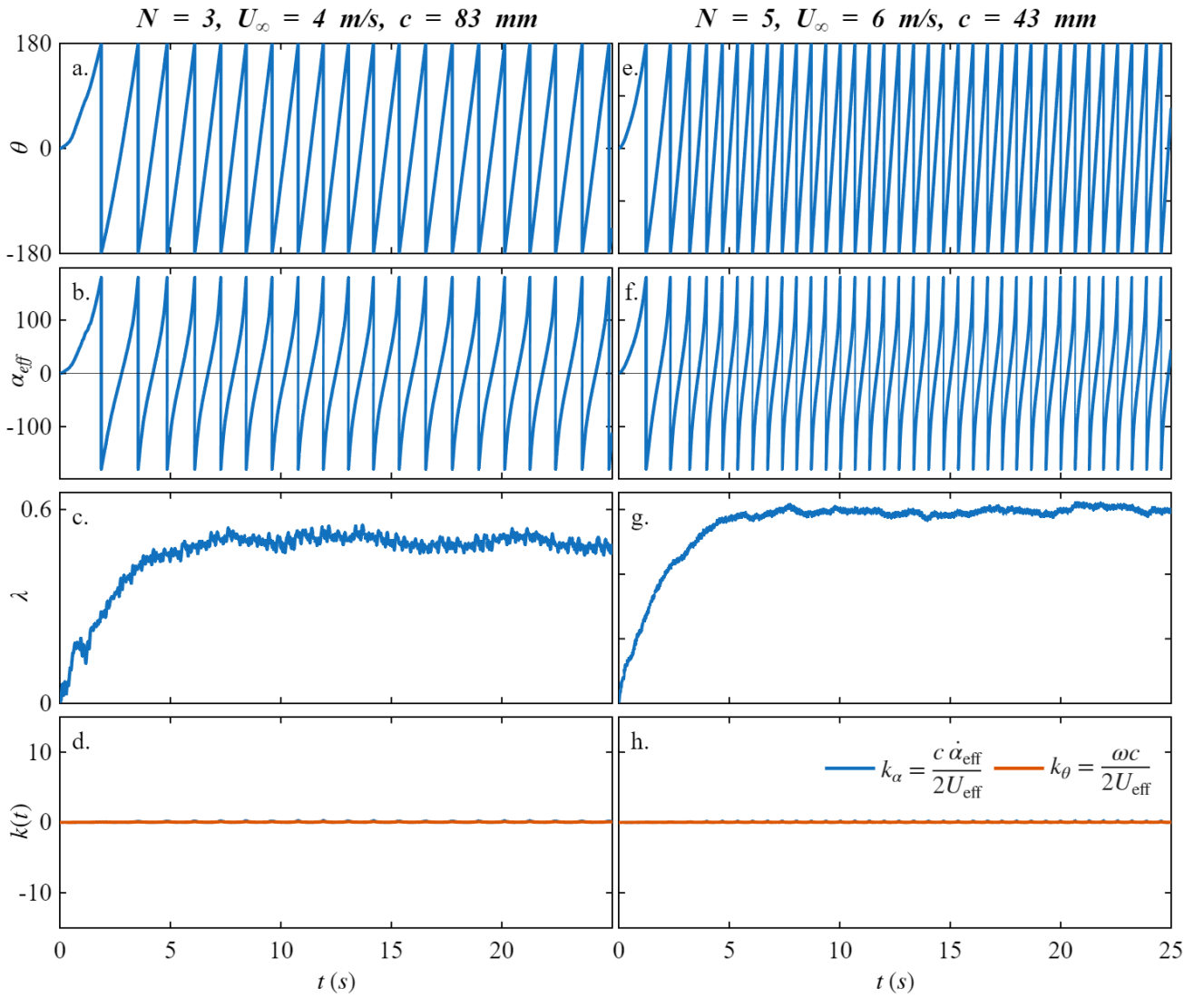


Figure 15: Single-blade kinematic time histories for two non-self-starting cases. Left column: $N = 3$, $c = 83$ mm, $U_\infty = 4$ m/s. Right column: $N = 5$, $c = 43$ mm, $U_\infty = 6$ m/s. Shown are (a,e) azimuthal position $\theta(t)$, (b,f) effective angle of attack $\alpha_{\text{eff}}(t)$, (c,g) tip-speed ratio $\lambda(t)$, and (d,h) reduced frequencies $k_\alpha(t)$ and $k_\theta(t)$

discussed previously, a reduced frequency of $k = 0.05$ is used as a reference level beyond which high levels of unsteadiness persist in the flow and unsteady aerodynamic effects become significant. This value is a commonly accepted indicator of strong unsteady behavior relevant to dynamic stall. From the two parameters, k_α and k_θ , to characterize motion of a VAWT, k_α is the primary parameter relevant to dynamic stall, as it directly reflects the rate of change of the effective angle of attack and governs the onset of flow reversal, shear-layer roll-up, and dynamic stall vortex formation [45, 47, 53]. On the other hand, k_θ characterizes unsteadiness associated with the rate of change of the azimuthal position. Due to this primary difference between the two reduced frequencies, the identification and analysis of dynamic stall events in the present work are based on intervals where $k_\alpha > 0.05$. Nevertheless, k_θ is reported to identify phases during which a blade experiences increase in angular speed and to provide information about the overall unsteady state of the turbine.

Based on a single blade's kinematics, our emphasis now is on determining whether it experiences elevated levels of unsteadiness uniformly throughout its rotational cycle. The plots in Fig. 16 demonstrates that it only undergoes these phases at distinct and localized intervals during its rotation. After Cycle 9 that corresponds to the onset of self-starting, k_α no longer exceeds the reference level. It directly hints that dynamic stall-related effects diminish significantly once the turbine escapes the

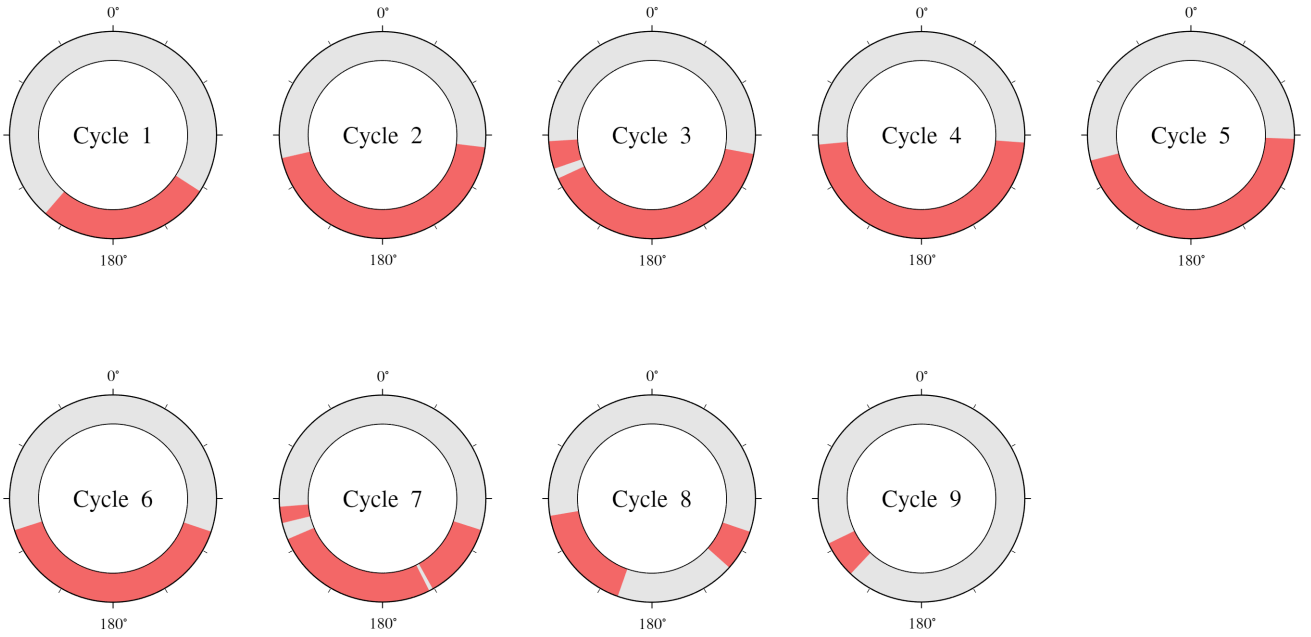


Figure 16: Annular maps of the pitching reduced frequency for $N = 3$, $c = 83$ mm, $U_\infty = 6$ m/s, k_α , over one revolution in azimuthal angle θ (0 – 360°) for Cycles 1–9. Shaded arc segments indicate azimuthal intervals where $k_\alpha > 0.05$, while unshaded portions correspond to $k_\alpha \leq 0.05$.

dead-band regime and accelerates to higher values of λ . Quite oppositely, k_θ exhibits an intermittent behavior during the early cycles but remains continuously elevated once self-starting is achieved, as shown in Fig. 17. These high values of k_θ demonstrates sustained azimuthal unsteadiness associated with the increasing rotational speed in the shaded regimes, as shown in Fig. 17.

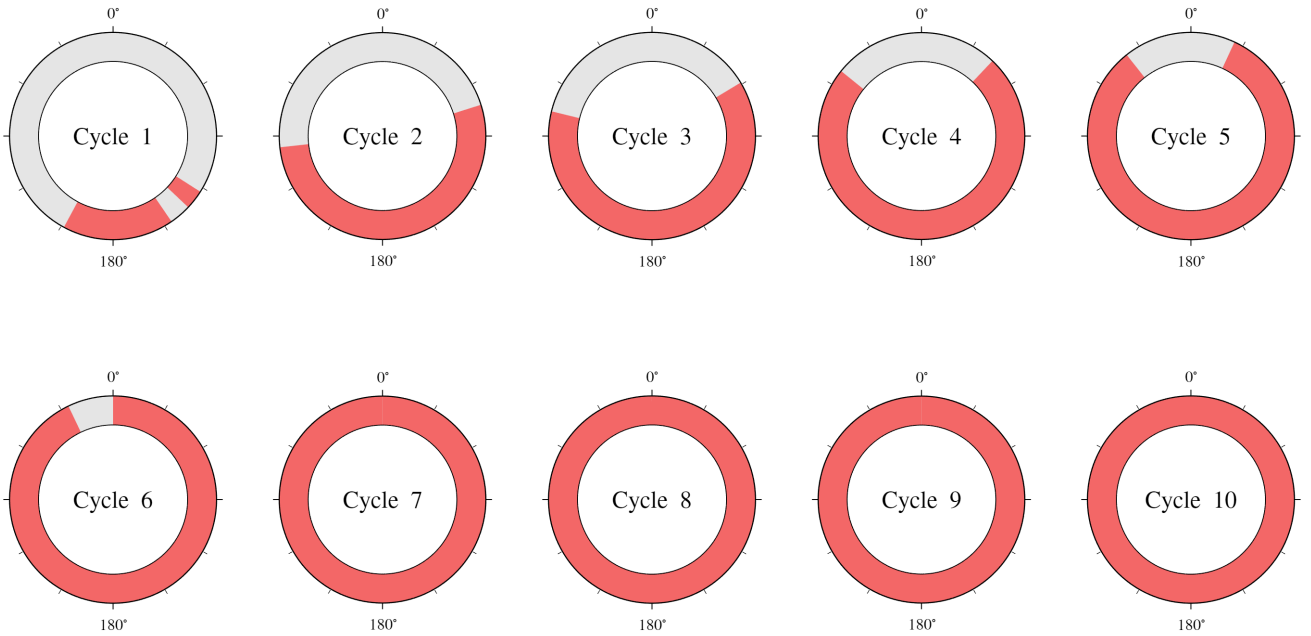


Figure 17: Annular maps of the azimuthal reduced frequency, k_θ , for $N = 3$, $c = 83$ mm, $U_\infty = 6$ m/s over one revolution in azimuthal angle θ (0 – 360°) for Cycles 1–10. Shaded arc segments indicate azimuthal intervals where $k_\theta > 0.05$.

The unsteady behavior of the remaining blades can be determined by incorporating the appropriate azimuthal phase shift in the analysis. As λ increases in successive cycles, the phase-shifted blades experience larger effective inflow velocities, leading to amplified reduced frequencies. This behavior is illustrated in Fig. 18, where Blade 3, which is the last one in the phase sequence, exhibits very large

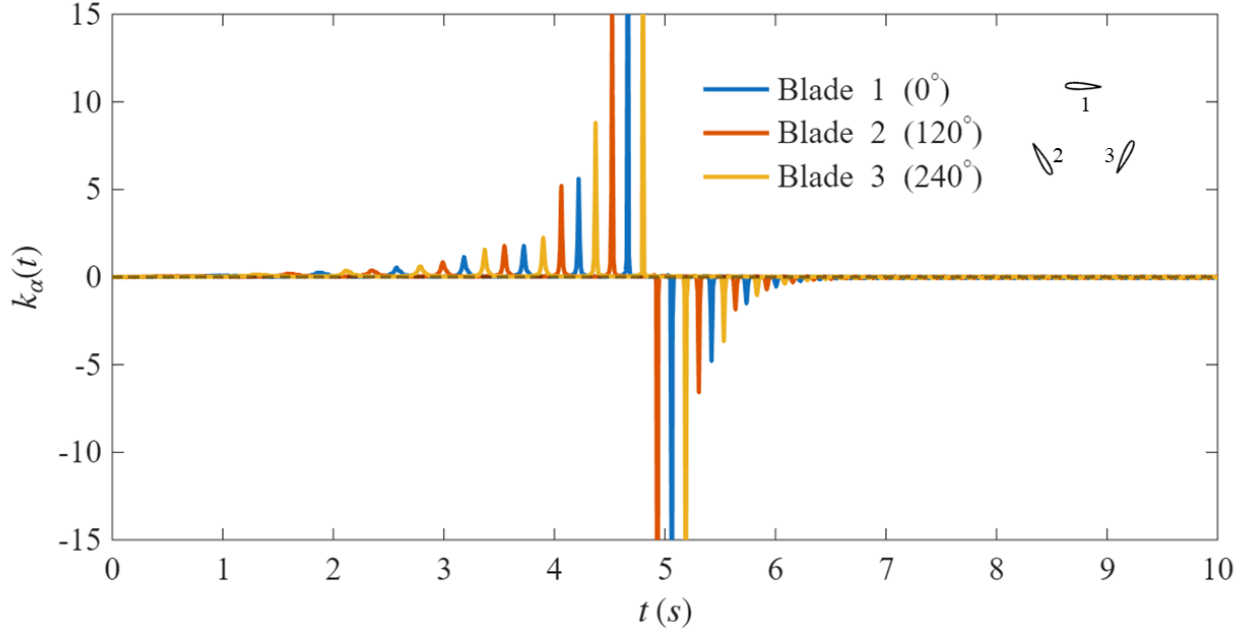


Figure 18: Collective time history of the pitching reduced frequency, $k_\alpha(t)$, for $N = 3$, $c = 83$ mm, $U_\infty = 6$ m/s

transient values of k_α . These large magnitudes arise from the rapid increase in effective inflow velocity with an increasing λ , which amplifies the normalized response even for modest variations in the $\dot{\alpha}_{eff}$ pitching rate.

The identified k_α intervals therefore represent the most physically meaningful windows for analyzing dynamic stall in a turbine, experiencing flow-induced rotational acceleration. Within these intervals, a blade's kinematics closely resemble those of an airfoil undergoing dynamic stall under prescribed unsteady motion, as widely reported in the literature [47, 52, 54, 55]. Importantly, dynamic stall does not occur continuously throughout the startup process, but only during specific phases of the rotation. Similar behaviour were reported by Selvarajoo and Kassim [56], who observed that dynamic stall events occurred only within limited intervals associated with elevated pitching rates. Vorticity analysis performed during a representative k_α interval further confirms this interpretation. As shown in Fig. 19, the classical sequence of subprocesses involved in dynamic stall is observed: (i) the formation of DSV in Fig. 19a, (ii) its progressive growth as it is fed by the separated shear layer in Fig. 19b, (iii) destabilization through the development of oppositely signed vorticity between the vortex and the blade surface shown in Fig. 19c, and (iv) its eventual detachment from the blade illustrated in Fig. 19d. The detached vortex subsequently convects downstream, as depicted by Fig. 19e. These observations demonstrate that, despite the freely rotating nature of the turbine, the underlying dynamic stall mechanism remains consistent with that reported for airfoils undergoing prescribed oscillations.

3.2 Comparison of BVI and viscous moment effects in self-starting cases

To quantify the role of BVI during self-starting, two representative cases of 3- and 5-bladed VAWTs with $c = 83$ mm are examined at $U_\infty = 6$ m/s. The instantaneous vorticity fields are compared in Fig. 20, where the left column (Figs. 20a–20d) corresponds to the 3 blade case, and the right column (Figs. 20i–20iv) corresponds to the 5-bladed turbine. Please note that both turbine could self start, as identified in Fig. 7. Both configurations exhibit strong vortex shedding during the early stages, consistent with the initially stalled state, large excursions of α_{eff} , and the absence of an established

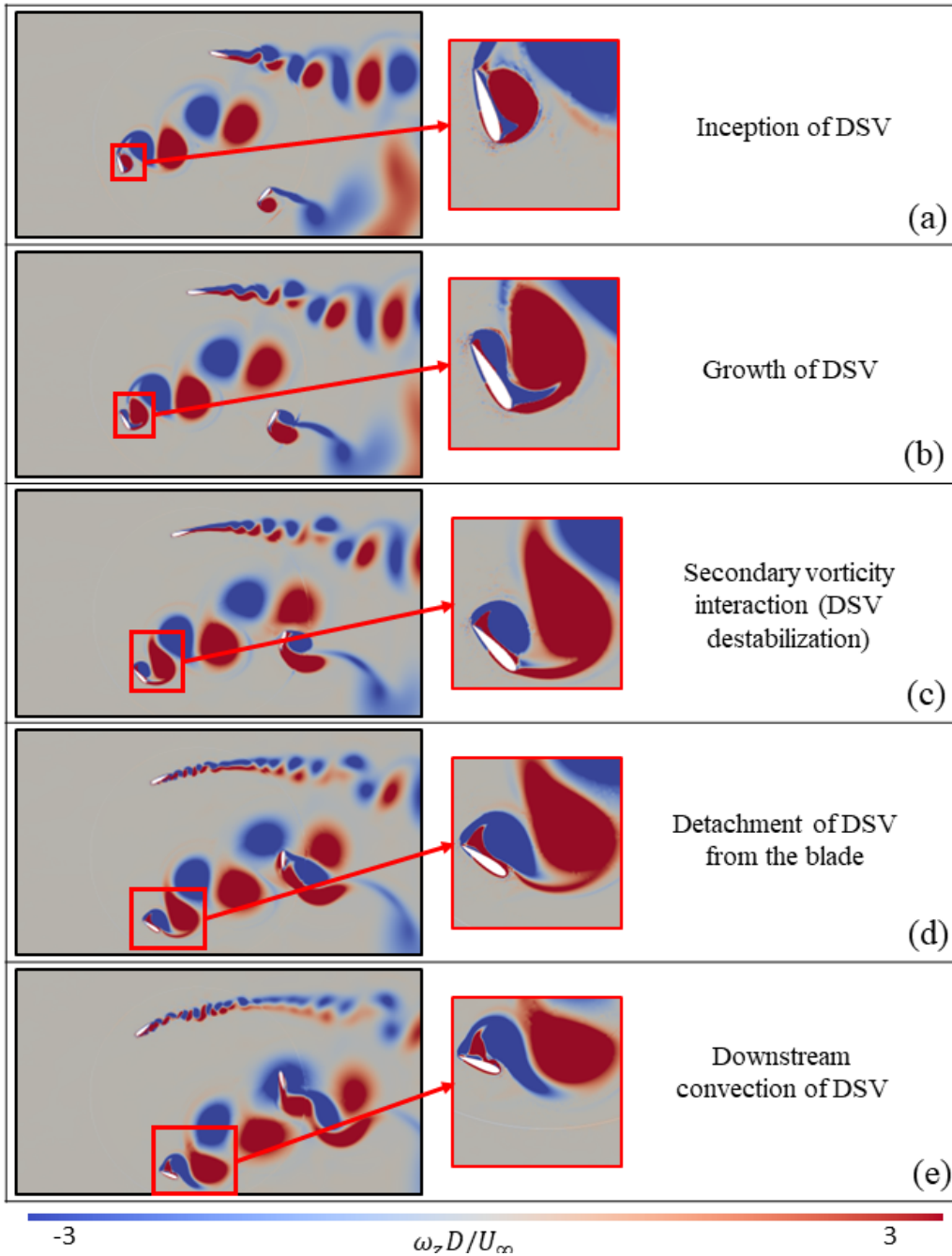


Figure 19: Evolution of the dynamic stall vortex (DSV) during Cycle 4 for $N = 3$ at $U_\infty = 6$ m/s and $c = 83$ mm, visualized using normalized spanwise vorticity, $\omega_z D / U_\infty$

wake (Figs. 20(a)- 20(i)). The shed vortices convect to the downstream half of the rotor and interact with the blades later in the cycle. This interaction is undesirable, because it perturbs the local flow, approaching the blade. It can reduce the effectiveness of torque production during startup and increase structural loading [6, 15–17, 57].

Figures 20a–20i illustrates the early low- λ regime, where large, coherent vortices are shed and convected across the rotor. In this phase, the downstream half-cycle contains energetic flow structures, increasing the likelihood of strong BVI there. At a moderate λ shown in Fig. 20b and 20ii, the near-blade shear layer becomes more organized and the most energetic large-scale shedding events become less frequent. During the subsequent acceleration phase (Figs. 20c and 20iii), the wake breaks into smaller-scale structures and downstream interactions in the second half-cycle become less frequent. It may happen because the convected flow structures reaching the downwind passage are weaker and more fragmented. Once self-starting is achieved (Fig. 20d and 20iv), the flow field is dominated by a

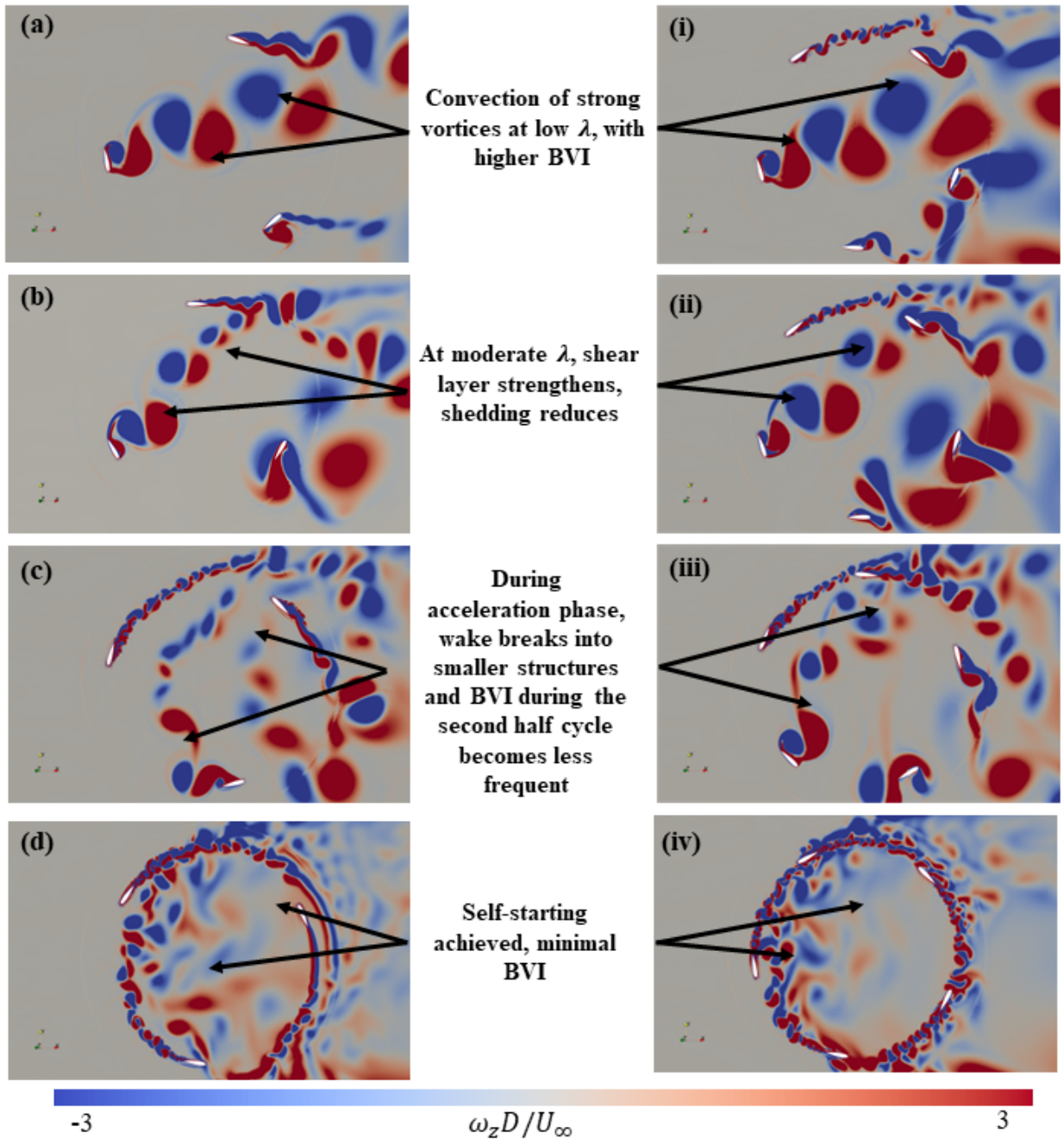


Figure 20: Evolution of vortex development and BVI during self-starting at $c = 83$ mm and $U_\infty = 6$ m/s, comparing $N = 3$ (left column, a–d) and $N = 5$ (right column, i–iv).

more established wake with reduced large-scale shedding, and only limited downstream interaction is apparent. A clear distinction between the two configurations in Fig. 20 is the degree of downstream interaction across the same phases. The 5-bladed rotor occupies a larger fraction of the azimuth at any instant, and therefore has a higher probability of encountering vortical structures convected from the upstream half-cycle. It increases the frequency and severity of downstream interactions compared to those for a 3-bladed rotor. Consequently, although additional blades can be beneficial in the start-up stage, the increased likelihood of downstream blade-vortex interactions can contribute to a lower attainable steady λ when the turbine transitions out of the dead band.

Besides, the same mechanism also explains the influence of chord on the underlying unsteady fluid dynamics around the rotors in a general sense. Increasing c enhances the spatial footprint of blade-associated separated-flow regions and the size of the shed vortical structures. It also increases the probability of intersecting convected vorticity in the downstream half-cycle due to a large part of the

periphery covered by the blades. Consequently, even for cases that do self-start, larger chord lengths tend to experience a stronger BVIs during recovery and post-startup, which can penalize the final steady λ . This interpretation motivates examining the relative roles of pressure-driven and viscous contributions to the net moment of the whole turbines around their axis of rotation. The two components of the aerodynamic moment are shown in Fig. 21 for a 3- and a 5-bladed turbine with blades of $c = 43$ mm at $U_\infty = 8$ m/s. These two cases are selected because, for each blade count, they reach the maximum λ_{steady} following the transient acceleration phase, and therefore provide a consistent basis for comparing the torque balance at the highest attainable operating state. From Fig. 21, the mean viscous contribution to M_z is more negative for the 5-bladed turbine than for its 3-blades counterpart. Their time-averaged values are -0.48 and -0.33 , respectively. As a result, a larger fraction of the available driving moment primarily relates to skin-friction and near-wall shear effects, which reduces the net torque available to sustain rotation for the turbine. Consequently, the 5-bladed VAWT attains a lower λ_{steady} than the 3-bladed one under the same operating flow parameters. During the early startup and dead-band evolution, the viscous contribution remains small relative to the pressure-driven moment, while the pressure-driven moment exhibits strong fluctuations and frequent sign changes consistent with repeated separation/recovery and interaction events. As the turbines transitions into sustained acceleration, the pressure-driven moment becomes persistently positive and increases sharply. After sustained rotation is established, the viscous contribution becomes clearly non-negligible and remains predominantly negative, which indicates that viscous stresses act as an aerodynamic braking mechanism in order to limit further increase in the angular speed of the VAWT.

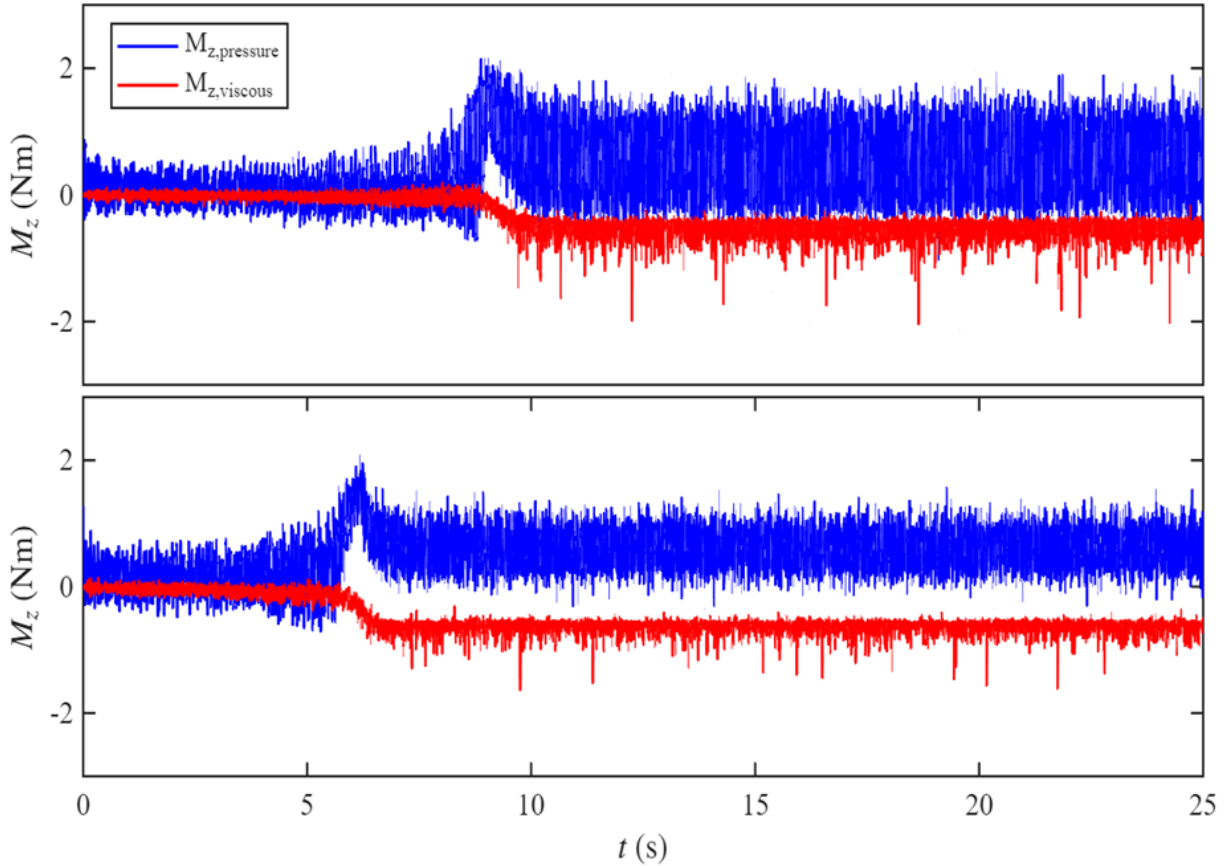


Figure 21: Decomposition of the axial moment into pressure-driven and viscous contributions for a 3-bladed turbine (upper) and a 5-bladed turbine (lower) with blades of $c = 43$ mm at $U_\infty = 8$ m/s

4 Conclusions

This study examines the influence of c and N on the self-starting behavior and steady operating state of a Darrieus-type VAWT using two-dimensional URANS simulations of freely accelerating rotors. EC and ES configuration families are analyzed to isolate the individual and combined effects of c and N on startup dynamics, unsteady aerodynamics, and the attainable λ_{steady} .

The results indicate that geometric parameters influence self-starting indirectly, while the decisive factor is the persistence of organized unsteady aerodynamic loading capable of producing cumulative positive torque. For both the 3 blade and 5 blade configurations at constant R and J , self-starting occurs only above c_{crit} , below which the turbine remains trapped in the dead-band regime with $\lambda_{\text{steady}} < 1$. The existence of c_{crit} therefore defines a clear geometric threshold separating non-self-starting and self-starting behavior. Increasing the blade number shifts this threshold to larger values of c , indicating that a greater chord is required to sustain the level of unsteadiness necessary for startup. In the ES family, this shift becomes sufficiently strong that self-starting is suppressed entirely, demonstrating that increasing N under comparable operating conditions is detrimental to sustained rotation.

The dynamic stall analysis shows that, in a freely accelerating VAWT, dynamic stall is not sustained throughout startup but occurs intermittently over localized azimuthal intervals associated with elevated pitching unsteadiness. The reduced frequency k_α emerges as the primary parameter governing dynamic stall activity, as it directly reflects the rate of change of α_{eff} and controls the onset of flow reversal, shear-layer roll-up, and dynamic stall vortex formation. Exceeding the unsteady limit alone is insufficient to induce dynamic stall, rather, sustained intervals of elevated k_α are required to allow the separated shear layer to evolve into a coherent vortex structure. During the early startup and dead-band phases, intermittent dynamic stall events are observed, while their magnitude and duration diminish as the turbine accelerates and transitions toward sustained rotation. Once self-starting is achieved, k_α remains below the unsteady threshold, indicating that dynamic stall is suppressed at higher operating states, even though k_θ may remain elevated. These results demonstrate that dynamic stall in a freely rotating VAWT is governed by the temporal organization of pitching-rate unsteadiness rather than by instantaneous angle of attack alone, and that reduced-frequency measures provide a physically meaningful framework for identifying and analyzing dynamic stall activity during startup.

Vorticity contours analysis demonstrate that vortices generated during the upwind half-cycle convect into the downwind half and interact with subsequent blades, producing resistive loading through BVI. The frequency and severity of this interaction increase with blade number and chord length, providing a consistent physical explanation for the reduction in λ_{steady} observed for 5 blade turbines and for larger-chord configurations that do self-start.

The moment decomposition shows that viscous effects play an active role in the self-starting process. While viscous contributions are small during the earliest stages, they become dynamically significant during the acceleration phase and remain predominantly negative once sustained rotation is established. At the highest attainable operating states, the 5 blade turbine exhibits a more negative mean viscous contribution than the 3 blade turbine, indicating stronger viscous dissipation and reduced net torque availability. This increased viscous dominance directly limits the attainable λ_{steady} .

From a design perspective, the results demonstrate a clear startup–performance trade-off. Increasing c or N promotes early-stage unsteady loading and facilitates escape from the dead band, but simultaneously increases BVI and viscous losses that limit the steady operating state. The identification of a critical chord length and the use of reduced-frequency metrics provide practical tools for diagnosing startup capability and dynamic stall activity. These tools offer a physically grounded framework through which future geometric modifications, such as changes in chord distribution, blade count, or airfoil selection, can be assessed and guided toward improved self-starting performance without compromising steady-state efficiency.

Although the present results are obtained from two-dimensional URANS simulations, the observed relationships between critical chord length, sustained unsteadiness, reduced-frequency behaviour, BVI, and viscous moment contribution remain consistent across the parameter space considered. The find-

ings therefore provide design relevant insight into the mechanisms governing self-starting and steady operation in lift-driven VAWTs, and establish a foundation for future three-dimensional and experimentally coupled investigations.

Acknowledgment

MSU Khalid acknowledges the funding support from Lakehead University through the startup grant and the Natural Sciences and Engineering Research Council of Canada (NSERC) through the Discovery grant program. F. Muhammad is thankful to Lakehead University for the graduate scholarship and for the support through the Ontario Graduate Scholarship. The simulations reported in this work were performed on the supercomputing clusters administered and managed by the Digital Research Alliance of Canada.

References

- [1] Ion Paraschivoiu. *Wind turbine design: with emphasis on Darrieus concept*. Presses inter Polytechnique, 2002.
- [2] M Khudri Johari, Muhd Jalil, and Mohammad Faizal Mohd Shariff. Comparison of horizontal axis wind turbine (hawt) and vertical axis wind turbine (vawt). *International Journal of Engineering and Technology*, 7(4.13):74–80, 2018.
- [3] Victor Mendoza, Ashvinkumar Chaudhari, and Anders Goude. Performance and wake comparison of horizontal and vertical axis wind turbines under varying surface roughness conditions. *Wind Energy*, 22(4):458–472, 2019.
- [4] Rakesh Kumar, Kaamran Raahemifar, and Alan S Fung. A critical review of vertical axis wind turbines for urban applications. *Renewable and Sustainable Energy Reviews*, 89:281–291, 2018.
- [5] Scheaua Fanel Dorel, Goanta Adrian Mihai, and Dragan Nicusor. Review of specific performance parameters of vertical wind turbine rotors based on the savonius type. *Energies*, 14(7):1962, 2021.
- [6] Sébastien Le Fouest and Karen Mulleners. Optimal blade pitch control for enhanced vertical-axis wind turbine performance. *Nature Communications*, 15(1):2770, 2024.
- [7] Haitian Zhu, Wenxing Hao, Chun Li, and Qinwei Ding. Numerical study of effect of solidity on vertical axis wind turbine with gurney flap. *Journal of Wind Engineering and Industrial Aerodynamics*, 186:17–31, 2019.
- [8] Antonio Posa. Secondary flows in the wake of a vertical axis wind turbine of solidity 0.5 working at a tip speed ratio of 2.2. *Journal of Wind Engineering and Industrial Aerodynamics*, 213:104621, 2021.
- [9] Lining Zhu, Erhu Hou, Qingwei Zhou, and He Wu. Numerical experiments on hydrodynamic performance and the wake of a self-starting vertical axis tidal turbine array. *Journal of Marine Science and Engineering*, 10(10):1361, 2022.
- [10] Zhenyu Kong, Donghai Zhou, and Xiaojing Sun. Improvement of self-starting and power extraction performance of an H-type vertical-axis hydrokinetic turbine by partial deflection of its blades. *Ocean Engineering*, 296:116855, 2024.
- [11] Majid Zare Chavoshi and Abbas Ebrahimi. Self-starting and performance improvement of a Darrieus type wind turbine using the plasma actuator. *Physics of Fluids*, 36(5), 2024.

- [12] Muhammad Saif Ullah Khalid, David Wood, and Arman Hemmati. Self-starting characteristics and flow-induced rotation of single-and dual-stage vertical-axis wind turbines. *Energies*, 15(24):9365, 2022.
- [13] Manabu Takao, Hideki Kuma, Takao Maeda, Yasunari Kamada, Michiaki Oki, and Atsushi Minoda. A straight-bladed vertical axis wind turbine with a directed guide vane row—effect of guide vane geometry on the performance—. *Journal of thermal Science*, 18(1):54–57, 2009.
- [14] Norman D Ham and Melvin S Garelick. Dynamic stall considerations in helicopter rotors. *Journal of the American Helicopter Society*, 13(2):49–55, 1968.
- [15] D De Tavernier, Carlos Ferreira, A Viré, B LeBlanc, and S Bernardy. Controlling dynamic stall using vortex generators on a wind turbine airfoil. *Renewable Energy*, 172:1194–1211, 2021.
- [16] Reeve Dunne and Beverley J McKeon. Dynamic stall on a pitching and surging airfoil. *Experiments in Fluids*, 56(8):157, 2015.
- [17] Pablo Ouro, Thorsten Stoesser, and Luis Ramírez. Effect of blade cambering on dynamic stall in view of designing vertical axis turbines. *Journal of Fluids Engineering*, 140(6):061104, 2018.
- [18] Mark A Miller, Subrahmanyam Duvvuri, and Marcus Hultmark. Solidity effects on the performance of vertical-axis wind turbines. *Flow*, 1:E9, 2021.
- [19] MH Mohamed. Impacts of solidity and hybrid system in small wind turbines performance. *Energy*, 57:495–504, 2013.
- [20] A Sagharichi, M Zamani, and Am Ghasemi. Effect of solidity on the performance of variable-pitch vertical axis wind turbine. *Energy*, 161:753–775, 2018.
- [21] Shoutu Li, Ye Li, Congxin Yang, Qiang Wang, Bin Zhao, Deshun Li, Ruiwen Zhao, Tongxin Ren, Xiaobo Zheng, Zhiteng Gao, et al. Experimental investigation of solidity and other characteristics on dual vertical axis wind turbines in an urban environment. *Energy Conversion and Management*, 229:113689, 2021.
- [22] Kevin W McLaren. *A numerical and experimental study of unsteady loading of high solidity vertical axis wind turbines*. PhD thesis, McMaster University, Hamilton, Ontario, Canada, 2011.
- [23] Guoqiang Tong, Yan Li, Kotaro Tagawa, and Fang Feng. Effects of blade airfoil chord length and rotor diameter on aerodynamic performance of straight-bladed vertical axis wind turbines by numerical simulation. *Energy*, 265:126325, 2023.
- [24] Nathaniel J Wei, Ian D Brownstein, Jennifer L Cardona, Michael F Howland, and John O Dabiri. Near-wake structure of full-scale vertical-axis wind turbines. *Journal of Fluid Mechanics*, 914:A17, 2021.
- [25] J Rainbird. The aerodynamic development of a vertical axis wind turbine. *Master's thesis, University of Durham, Durham, UK*, 2007.
- [26] Mahdi Torabi Asr, Erfan Zal Nezhad, Faizal Mustapha, and Surjatin Wiriadidjaja. Study on start-up characteristics of H-Darrieus vertical axis wind turbines comprising naca 4-digit series blade airfoils. *Energy*, 112:528–537, 2016.
- [27] Esmaeel Fatahian, Rakesh Mishra, Frankie F Jackson, and Hossein Fatahian. Optimization and analysis of self-starting capabilities of vertical axis wind turbine pairs: A cfd-taguchi approach. *Ocean Engineering*, 302:117614, 2024.

- [28] Alessandro Bianchini, Francesco Balduzzi, John M Rainbird, Joaquim Peiro, J Michael R Graham, Giovanni Ferrara, and Lorenzo Ferrari. An experimental and numerical assessment of airfoil polars for use in Darrieus wind turbines—part ii: Post-stall data extrapolation methods. *Journal of Engineering for Gas Turbines and Power*, 138(3):032603, 2016.
- [29] Yunus Celik, Derek Ingham, Lin Ma, and Mohamed Pourkashanian. Design and aerodynamic performance analyses of the self-starting H-type vawt having j-shaped aerofoils considering various design parameters using cfd. *Energy*, 251:123881, 2022.
- [30] Abdolrahim Rezaeiha, Ivo Kalkman, and Bert Blocken. Cfd simulation of a vertical axis wind turbine operating at a moderate tip speed ratio: Guidelines for minimum domain size and azimuthal increment. *Renewable energy*, 107:373–385, 2017.
- [31] Ye Zhang, Shuanghou Deng, and Xiaofang Wang. Rans and ddes simulations of a horizontal-axis wind turbine under stalled flow condition using openfoam. *Energy*, 167:1155–1163, 2019.
- [32] Timothy Stovall, Gary Pawlas, and Patrick Moriarty. Wind farm wake simulations in openfoam. In *48th AIAA aerospace sciences meeting including the new horizons forum and aerospace exposition*, page 825, 2010.
- [33] Yung-Jeh Chu and Wen-Tong Chong. A biomimetic wind turbine inspired by dryobalanops aromatica seed: Numerical prediction of rigid rotor blade performance with openfoam®. *Computers & Fluids*, 159:295–315, 2017.
- [34] Young Jun Kim, Moran Charlou, Benjamin Bouscasse, Vincent Leroy, Sithik Aliyar, Félicien Bonnefoy, Kyong-Hwan Kim, and Young-Myung Choi. High fidelity simulations of a floating offshore wind turbine in irregular waves by coupling openfoam and openfast. *Renewable Energy*, 243:122486, 2025.
- [35] Alessio Ricci. Review of openfoam applications in the computational wind engineering: from wind environment to wind structural engineering. *Meccanica*, 60(6):1695–1735, 2025.
- [36] Danh Nam Nguyen and Chun Sang Yoo. An openfoam-based solver for modeling low mach number turbulent flows at high pressure with real-fluid effects. *Computer Physics Communications*, 312:109600, 2025.
- [37] Olle Penttinen, Ehsan Yasari, and Håkan Nilsson. A pimplefoam tutorial for channel flow, with respect to different les models. *Practice Periodical on Structural Design and Construction*, 23(2):1–23, 2011.
- [38] Ayyoob Zarmehri, Nina Gall Jørgensen, and Jelena Andric. γ -re θ transitional turbulence model tutorial. *Proceedings of CFD with OpenSource Software*. [http://dx. doi. org/10.17196/OS_CFD#YEAR_2012](http://dx.doi.org/10.17196/OS_CFD#YEAR_2012), 2012.
- [39] Jose Miguel Ramirez and Martín Saravia. Assessment of reynolds-averaged navier–stokes method for modeling the startup regime of a Darrieus rotor. *Physics of Fluids*, 33(3), 2021.
- [40] Chao Li, Songye Zhu, You-lin Xu, and Yiqing Xiao. 2.5 d large eddy simulation of vertical axis wind turbine in consideration of high angle of attack flow. *Renewable energy*, 51:317–330, 2013.
- [41] Longhuan Du, Grant Ingram, and Robert G Dominy. A review of H-Darrieus wind turbine aerodynamic research. *Proceedings of the Institution of Mechanical Engineers, Part C: Journal of Mechanical Engineering Science*, 233(23-24):7590–7616, 2019.

- [42] Xuejing Sun, Jianyang Zhu, Zongjin Li, and Guoxing Sun. Rotation improvement of vertical axis wind turbine by offsetting pitching angles and changing blade numbers. *Energy*, 215:119177, 2021.
- [43] William J McCroskey, Lawrence W Carr, and Kenneth W McAlister. Dynamic stall experiments on oscillating airfoils. *Aiaa Journal*, 14(1):57–63, 1976.
- [44] KW McAlister, SL Pucci, WJ McCroskey, and LW Carr. An experimental study of dynamic stall on advanced airfoil section. volume 2: Pressure and force data. Technical report, 1982.
- [45] Sébastien Le Fouest, Julien Deparday, and Karen Mulleners. The dynamics and timescales of static stall. *Journal of Fluids and Structures*, 104:103304, 2021.
- [46] Gordon J Leishman. *Principles of helicopter aerodynamics with CD extra*. Cambridge university press, 2006.
- [47] Sébastien Le Fouest and Karen Mulleners. The dynamic stall dilemma for vertical-axis wind turbines. *Renewable Energy*, 198:505–520, 2022.
- [48] WA Timmer. Two-dimensional low-reynolds number wind tunnel results for airfoil naca 0018. *Wind engineering*, 32(6):525–537, 2008.
- [49] Christoph Stangfeld, Christopher L Rumsey, Hanns Mueller-Vahl, David Greenblatt, C Nayeri, and Christian O Paschereit. Unsteady thick airfoil aerodynamics: experiments, computation, and theory. In *45th AIAA Fluid Dynamics Conference*, page 3071, 2015.
- [50] Luca Damiola, Muhammad Faheem Siddiqui, Mark Charles Runacres, and Tim De Troyer. Influence of free-stream turbulence intensity on static and dynamic stall of a naca 0018 aerofoil. *Journal of Wind Engineering and Industrial Aerodynamics*, 232:105270, 2023.
- [51] N Hill, Robert Dominy, Grant Ingram, and J Dominy. Darrieus turbines: The physics of self-starting. *Proceedings of the Institution of Mechanical Engineers, Part A: Journal of Power and Energy*, 223(1):21–29, 2009.
- [52] CJ Simao Ferreira, Hester Bijl, Gerard van Bussel, and G Van Kuik. Simulating dynamic stall in a 2d vawt: modeling strategy, verification and validation with particle image velocimetry data. In *Journal of physics: conference series*, volume 75, page 012023. IOP Publishing, 2007.
- [53] Sébastien Le Fouest, Daniel Fernex, and Karen Mulleners. Time scales of dynamic stall development on a vertical-axis wind turbine blade. *Flow*, 3:E11, 2023.
- [54] William J McCroskey. The phenomenon of dynamic stall. Technical report, 1981.
- [55] CJ Simão Ferreira, Z Gao, Z Cheng, E Lourens, and A Metrikine. Dynamic analysis of a floating vertical axis wind turbine using the actuator cylinder flow theory.
- [56] Shaza Rae Selvarajoo and Zulfaa Mohamed-Kassim. The effects of dynamic stalls on the aerodynamics and performance of a Darrieus rotor during self-start. *Physics of Fluids*, 36(1), 2024.
- [57] Carlos Simão Ferreira, Gijs Van Kuik, Gerard Van Bussel, and Fulvio Scarano. Visualization by piv of dynamic stall on a vertical axis wind turbine. *Experiments in fluids*, 46(1):97–108, 2009.